J. Fluid Mech. (2021), *vol*. 924, A40, doi:10.1017/jfm.2021.667

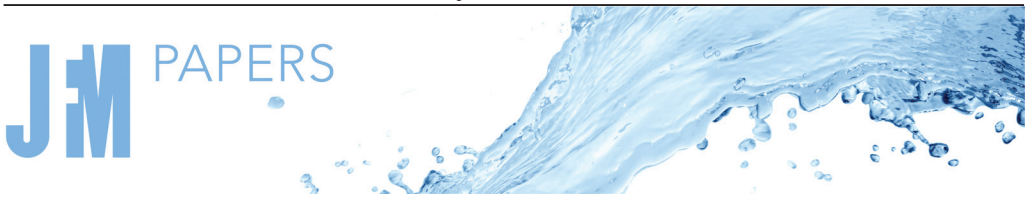

Investigation of three-scalar subgrid-scale mixing in turbulent coaxial jets

Wei Li[1], **Mengyuan Yuan**[1], **Campbell D. Carter**[2] **and Chenning Tong**[1],†

[1]Department of Mechanical Engineering, Clemson University, Clemson, SC 29634, USA

[2]Air Force Research Laboratory, Wright-Patterson Air Force Base, Dayton, OH 45433, USA

(Received 22 February 2021; revised 6 July 2021; accepted 19 July 2021)

Three-scalar subgrid-scale (SGS) mixing in turbulent coaxial jets is investigated experimentally. The flow consists of a centre jet, an annulus and a co-flow. The SGS mixing process and its dependence on the velocity and length scale ratios of the annulus flow to the centre jet are investigated. For small SGS scalar variance the scalars are well mixed and the initial three-scalar mixing configuration is lost. For large SGS variance, the scalars are highly segregated with a bimodal scalar filtered joint density function (f.j.d.f.) at a range of radial locations. Two competing factors, the SGS variance and the scalar length scale, play an important role for the bimodal f.j.d.f. For the higher velocity ratio cases, the peak value of the SGS variance is higher, thereby resulting in stronger bimodality. For the lower velocity ratio cases, the wider mean SGS variance profiles and the smaller scalar length scale cause bimodal f.j.d.f.s over a wider range of physical locations. The scalar dissipation rate structures have similarities to those of mixture fraction and temperature in turbulent non-premixed/partially premixed flames. The observed SGS mixing characteristics present a challenging test for SGS mixing models as well as provides an understanding of the physics for developing improved models. The results also provide a basis for investigating multiscalar SGS mixing in turbulent reactive flows.

Key words: turbulent mixing, turbulent reacting flows, turbulence modelling

1. Introduction

Scalar mixing is of great importance for understanding and modelling turbulent non-premixed flames. Mixing in such flows involves at least three scalars, e.g. two reactants and one product. While there is a large body of previous works, both experimental and numerical, on binary mixing (e.g. Warhaft & Lumley 1978; Sreenivasan *et al.* 1980; Antonopoulos-Domis 1981; Ma & Warhaft 1986; Eswaran & Pope 1988; Jayesh & Warhaft 1992; Tong & Warhaft 1995; Overholt & Pope 1996), multiscalar mixing has

† Email address for correspondence: ctong@clemson.edu

received much less attention. There are only a few previous studies on three-scalar mixing (e.g. Warhaft 1981; Sirivat & Warhaft 1982; Warhaft 1984; Tong & Warhaft 1995; Juneja & Pope 1996).

In three-scalar mixing, the initial scalar configuration, termed mixing configuration (Cai *et al.* 2011*b*), is of importance. To better understand the mixing process in turbulent non-premixed reactive flows, Cai *et al.* (2011*b*) and Li *et al.* (2017) studied three-scalar mixing in coaxial jets emanating into co-flow air. The mass fraction of the three streams, the centre jet (ϕ_1), the annular flow (ϕ_2) and the co-flow air (ϕ_3), represent the three scalars in this flow configuration. The three scalars are similar to the fuel, product and oxidizer in a non-premixed flame, respectively. Here ϕ_2 separates ϕ_1 and ϕ_3 in a similar way to the product separating the fuel and oxidizer, and mixing between ϕ_1 and ϕ_3 must involve ϕ_2. Cai *et al.* (2011*b*) found a curved diffusion manifold in scalar space, representing a 'detour' in the mixing path, which is difficult to capture using the current mixing models (Rowinski & Pope 2013).

Recently Li *et al.* (2017) further investigated the effects of mean shear and scalar initial length scale (annulus width) on the three-scalar mixing process. The results show that varying the velocity ratio can alter the mixing characteristics qualitatively. In particular, the joint probability density function (j.p.d.f.) for the higher velocity ratio cases is bimodal at some locations, while it is always unimodal for the lower velocity ratio cases. On the other hand, the annulus width only has quantitative effects on the mixing process. Increasing the velocity ratio and the annulus width always delays the evolution of the scalar fields. The evolution of the mean scalar profiles were found to be dominated by the mean-flow advection, while the shape of the j.p.d.f. is largely determined by the turbulent transport and molecular diffusion. The curvature of the diffusion manifold is significantly larger for the higher velocity ratio cases.

In the present study, we investigate three-scalar subgrid-scale (SGS) mixing in the context of large eddy simulation (LES) of turbulent reactive flows. In such LES the (joint) distribution of SGS scalars, i.e. the scalar filtered joint density function (f.j.d.f.), is needed in order to obtain the filtered reaction rates due to their nonlinear dependencies on the scalars. LES based on the filtered density function (f.d.f.) method has become a very promising approach (Colucci *et al.* 1998; Jaberi *et al.* 1999; Gicquel *et al.* 2002; Sheikhi *et al.* 2003, 2005; Raman, Pitsch & Fox 2005; Shetty, Chandy & Frankel 2010; Rowinski & Pope 2013). The LES-p.d.f. simulation of the three-scalar mixing problem by Rowinski & Pope (2013) showed that different mixing models have their limitations in capturing some of the key features such as the bimodal j.p.d.f. and the diffusion manifold. Much improvement in its capability to predict multiscalar mixing is still needed. Because the evolution of the f.j.d.f. depends strongly on the small-scale SGS mixing process, investigation of multiscalar SGS mixing is of importance.

Unlike j.p.d.f.s in Reynolds-averaged Navier–Stokes approaches, which are statistics, f.j.d.f.s in LES are still random variables, fluctuating both in time and space, and therefore can reveal much richer physics. LES therefore provides a new framework to investigate mixing. In the meantime, f.j.d.f.s and the related variables must be analysed using their statistics. Our previous studies (Tong 2001; Wang & Tong 2002; Rajagopalan & Tong 2003; Wang & Tong 2005; Wang *et al.* 2007*a*; Cai *et al.* 2009) have used the filtered mixture fraction and the SGS scalar variance as conditioning variables to obtain conditional means of these variables.

Previous studies have investigated the SGS (binary) mixing of the mixture fraction in turbulent jets and turbulent partially premixed flames (Tong 2001; Wang & Tong 2002; Rajagopalan & Tong 2003; Wang & Tong 2005; Wang *et al.* 2007*a*; Cai *et al.* 2009).

The f.d.f. of mixture fraction (a conserved scalar) in the jets and the filtered mass density function (f.m.d.f.) in the flames were analysed using their means conditioned on the resolvable-scale scalar and the SGS scalar variance. The results showed that the SGS scalar mixing has two limiting regimes. For instantaneous SGS variance values that are small compared with its mean, the conditional f.d.f is close to Gaussian, which indicates that the SGS scalar is well mixed. For large values of the SGS variance the conditional f.d.f. becomes bimodal, showing that on average the scalar within a grid cell consists of portions of well-mixed fluid that carry two distinct scalar values which are separated by a sharp interface (cliff). The results for the f.m.d.f. of the mixture fraction in turbulent flames also show similar trends (Wang *et al.* 2007*a*). Previous studies have also investigated multiscalar SGS mixing in turbulent partially premixed flames. The filtered joint mass density function (f.j.m.d.f.) of mixture fraction and temperature, and diffusion for large SGS variance have complex structures (Cai *et al.* 2009, 2011*a*; Liu & Tong 2013), and are influenced by both SGS mixing and reaction. It is therefore important to understand the effects of SGS mixing on the evolution of f.j.m.d.f.

In the present work we investigate three-scalar SGS mixing in the turbulent coaxial jets studied by Cai *et al.* (2011*b*) and Li *et al.* (2017). The scalar f.j.d.f. and the SGS mixing terms in the f.j.d.f. transport equation will be analysed to understand the physics of multiscalar SGS mixing. The f.j.d.f. is defined as (Pope 1990)

$$f(\hat{\phi}_1, \hat{\phi}_2; \boldsymbol{x}, t) = \langle \delta(\phi_1 - \hat{\phi}_1)\delta(\phi_2 - \hat{\phi}_2)\rangle_L = \int \delta(\phi_1 - \hat{\phi}_1)\delta(\phi_2 - \hat{\phi}_2) G(\boldsymbol{x} - \boldsymbol{x}')\, \mathrm{d}\boldsymbol{x}', \tag{1.1}$$

where ϕ_1, ϕ_2, $\hat{\phi}_1$ and $\hat{\phi}_2$ are the mixture fractions of the centre jet stream and the annular stream, and their sample-space variables, respectively. The filter function is denoted by G. We use the 'top-hat' (or box) filter in this study since it is simple and ensures positiveness of the f.j.d.f. The f.j.d.f. transport equation is

$$\begin{aligned} &\frac{\partial f}{\partial t} + \frac{\partial}{\partial x_i}\left[f\,\langle U_i|\,\hat{\phi}_1, \hat{\phi}_2\rangle_L\right] = -\frac{\partial}{\partial \hat{\phi}_1}\left[f\left\langle D_1\nabla^2\phi_1\middle|\,\hat{\phi}_1, \hat{\phi}_2\right\rangle_L\right] \\ &-\frac{\partial}{\partial \hat{\phi}_2}\left[f\left\langle D_2\nabla^2\phi_2\middle|\,\hat{\phi}_1, \hat{\phi}_2\right\rangle_L\right] = (D_1 + D_2)\nabla^2 f - \frac{1}{2}\frac{\partial^2}{\partial \hat{\phi}_1^2}\left[f\,\langle \chi_1|\,\hat{\phi}_1, \hat{\phi}_2\rangle_L\right] \\ &-\frac{1}{2}\frac{\partial^2}{\partial \hat{\phi}_2^2}\left[f\,\langle \chi_2|\,\hat{\phi}_1, \hat{\phi}_2\rangle_L\right] - \frac{\partial^2}{\partial \hat{\phi}_1 \partial \hat{\phi}_2}\left[f\,\langle \chi_{12}|\,\hat{\phi}_1, \hat{\phi}_2\rangle_L\right], \end{aligned} \tag{1.2}$$

where

$$U_i, \quad \chi_1 = 2D_1\frac{\partial \phi_1}{\partial x_i}\frac{\partial \phi_1}{\partial x_i}, \quad \chi_2 = 2D_2\frac{\partial \phi_2}{\partial x_i}\frac{\partial \phi_2}{\partial x_i}, \quad \text{and} \quad \chi_{12} = (D_1 + D_2)\frac{\partial \phi_1}{\partial x_i}\frac{\partial \phi_2}{\partial x_i} \tag{1.3}$$

are the velocity vector, the scalar dissipation rates and the cross-dissipation rate, respectively. The diffusion coefficients for ϕ_1 and ϕ_2, D_1 and D_2, have values of $0.1039\ \mathrm{cm^2\,s^1}$ and $0.1469\ \mathrm{cm^2\,s^{-1}}$, respectively (Reid, Prausnitz & Poling 1989). The left-hand side of (1.2) is time rate of change of the f.j.d.f. and transport of the f.j.d.f. in physical space by the conditionally filtered velocity. The right-hand side gives two forms of the mixing terms. The first involves two terms that can be interpreted as transport of f.j.d.f. in the scalar space, with the conditionally filtered diffusion $\langle D_1\nabla^2\phi_1|\hat{\phi}_1, \hat{\phi}_2\rangle_L$ and $\langle D_2\nabla^2\phi_2|\hat{\phi}_1, \hat{\phi}_2\rangle_L$ as the transport velocity components in the ϕ_1

and ϕ_2 directions, respectively. The second form involves four terms, which are transport of f.j.d.f. in physical space by molecular diffusion, and transport in scalar space by the conditionally filtered dissipation rates and by the conditionally filtered cross-dissipation rate. We will use filtered ϕ_1 and the SGS variance of ϕ_1 as conditioning variables to analyse the f.j.d.f. and the conditionally filtered terms.

In the present study, planar scalar images acquired in the turbulent coaxial jets using planar laser-induced fluorescence (PLIF) and planar laser Rayleigh scattering (Li *et al.* 2017) are used to obtain the statistics of the f.j.d.f., the conditionally filtered diffusion, the conditionally filtered dissipation and the conditionally filtered cross-dissipation. Two-dimensional filters are used to obtain the resolvable and SGS variables. The scalar diffusion and dissipation are calculated using scalar derivatives (two components) in the measurement plane. The rest of the paper is organized as follows. Section 2 describes the experimental set-up and data analysis procedures. Section 3 presents the results and is followed by the conclusions in § 4.

2. Flow configurations and experimental data

The experimental data used in the present study were the same as those of Li *et al.* (2017). Therefore, here we only summarize the flow configurations. Details of the experimental set-up and data reduction procedures have been reported by Li *et al.* (2017) and Cai *et al.* (2011*b*). The coaxial jets consisted of two round tubes of different diameters placed concentrically (figure 1), which resulted in a three-stream configuration. The mass fractions of the scalars emanating from the three streams are denoted as ϕ_1, ϕ_2 and ϕ_3, respectively, the sum of which is therefore unity. The centre stream, ϕ_1, is unity at the centre jet exit, while the annular stream, ϕ_2, is unity at the annular flow exit. The co-flow air represents the third scalar, ϕ_3.

Two coaxial jet assemblies with the same centre tube but different outer tubes were constructed (the jet dimensions are listed in table 1), with the smaller one having identical dimensions to those used by Cai *et al.* (2011*b*) (see that paper for the details of the construction). The jet assembly with the smaller annulus had a centre tube and an annulus tube of 545 mm and 470 mm in length, respectively. Three M1.5 set screws were placed 255 mm from the exit to make the tubes concentric. The larger jet assembly had tubes of lengths 570 mm and 490 mm, respectively, with the set screws placed at the same location. The centre stream was air seeded with approximately 9 % of acetone by volume, while the annular stream was pure ethylene. The densities of the centre stream and the annular stream were approximately 1.09 and 0.966 times the air density. The difference was sufficiently small for the scalars to be considered as dynamically passive. To monitor the pulse-to-pulse fluctuations of the laser energy, the laser intensity profile across the image height and the acetone seeding concentration for normalization, a laminar flow reference jet, which was picked off from the main jet using a T-adapter, was placed at approximately 0.5 m upstream of the main jet along the laser beam path.

For each coaxial jet assembly, measurements were made for the same centre jet (bulk) velocity with two annular flow (bulk) velocities, resulting in a total of four coaxial jet flows (table 2). The velocity ratio of the annular flow to the centre jet was close to unity for Cases I and III while it was approximately 0.5 for Cases II and IV. The velocities and Reynolds numbers of the four cases are listed in table 2. Note that Case I was identical to the flow studied by Cai *et al.* (2011*b*). The Reynolds numbers were calculated as $Re_j = U_{jb}D_{ji}/\nu_{air}$ and $Re_a = U_{ab}(D_{ai} - (D_{ji} + 2\delta_j))/\nu_{eth}$, where $\nu_{air} = 1.56 \times 10^{-5}$ m^2 s^{-1} and

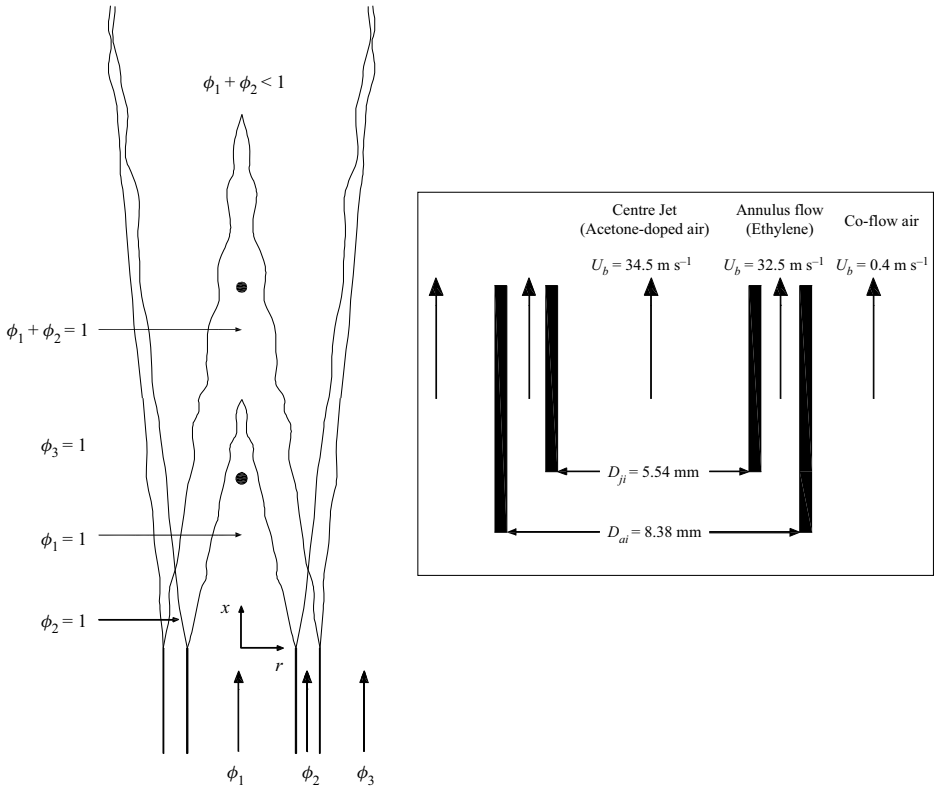

Figure 1. Schematic of the coaxial jet for Case I. The dimensions of jet tubes and the bulk velocities for other cases are listed in tables 1 and 2. The two solid circles represent the approximate downstream locations from where the cross-stream results are obtained that are reported in § 3.

	Inner tube		Annulus (outer) tube	
	D_{ji} (mm)	δ_j (mm)	D_{ai} (mm)	δ_a (mm)
Coaxial Jet I	5.54	0.406	8.38	0.559
Coaxial Jet II	5.54	0.406	10.92	0.889

Table 1. Dimensions of the coaxial jets. Here D_{ji}, δ_j and D_{ai}, δ_a are the inner diameter and the wall thickness of the inner tube and the annulus tube, respectively.

$\nu_{eth} = 0.86 \times 10^{-5}$ m^2 s^{-1} (Prausnitz, Poling & O'Connell 2001) are the kinematic viscosities of air and ethylene, respectively.

The coaxial jets were designed to have dimensions and Reynolds numbers comparable to the Sandia Flames D and E. While the Reynolds numbers of the Sandia flames D–E range from 22 000 to 36 000, they are based on the cold jet fluid. In the flames the diffusivity is higher, which leads to larger dissipation length scales and lower effective Reynolds numbers. For example, the smallest scalar (mixture fraction) dissipation length scale for flame E is approximately 65 μm (Wang, Karpetis & Barlow 2007*b*) larger than that in the coaxial jets. Therefore, the Reynolds numbers of the coaxial jets are closer to the effective Reynolds numbers in the Sandia flames than the cold-flow Reynolds numbers suggest.

	Jet	U_{jb} (m s^{-1})	Re_j	U_{ab} (m s^{-1})	Re_a	Velocity ratio $\frac{U_{ab}}{U_{jb}}$
Case I	Jet I	34.5	12 190	32.5	7636	0.94
Case II	Jet I	34.5	12 190	16.3	3818	0.47
Case III	Jet II	34.5	12 190	32.5	17 263	0.94
Case IV	Jet II	34.5	12 190	16.3	8631	0.47

Table 2. Characteristics of the coaxial jets. Here U_{jb} and U_{ab} are the bulk velocities of the centre stream and the annular stream, respectively. The Reynolds numbers are calculated using the tube diameter D_{ji} and the hydraulic diameter of the annulus $D_{ai} - (D_{ji} + 2\delta_j)$.

Simultaneous PLIF and planar laser Rayleigh scattering were employed to measure the mass fractions of the acetone-doped air (ϕ_1) and ethylene (ϕ_2). The experimental set-up (figure 2) was similar to that of Cai *et al.* (2011*b*). The second harmonic (532 nm) of a Q-switched Nd:YAG laser (Quanta-Ray LAB-170 operated at 10 pulses s^{-1}) having a pulse energy of approximately 325 mJ was used for Rayleigh scattering. The fourth harmonic (266 nm) of another Q-switched Nd:YAG laser (Quanta-Ray PRO-350 also operated at 10 pulses s^{-1}) was used for acetone PLIF, with a pulse energy of approximately 80 mJ pulse^{-1}. The second (532 nm) and the fourth harmonics (266 nm) of a Q-switched Nd:YAG laser were used for Rayleigh scattering and LIF, respectively. The height of the laser sheets were approximately 40 mm and 60 mm, respectively, for the 532 nm beam and the 266 nm beam. However, only the centre 12 mm portion having a relative uniform intensity was imaged. A Cooke Corp. PCO-1600 interline-transfer CCD camera was used to collect both LIF and Rayleigh signals. The LIF and Rayleigh images of the reference jet were recorded with two Andor ICCDs (both were iStar 334T), placed face to face on either side of the laser sheet. The images were not intensified.

The PLIF signal was linearly proportional to the laser intensity and acetone mole fraction, while the Rayleigh scattering signal was linearly proportional to the laser intensity and the effective Rayleigh cross-section, which was a mole-weighted average of the Rayleigh cross-section of the three species in the flow (acetone, ethylene and air). With these relationships and the fact that mass fractions of the three scalars sum to unity, the three mass fractions could be obtained from the PLIF and Rayleigh scattering signals. More details about the data reduction procedures have been reported by Cai *et al.* (2011*b*). The background signals were subtracted from both the main camera images and the reference jet images (Li *et al.* 2017). The background images were taken with pure helium emanating from a McKenna burner and lasers operating normally, because helium does not have LIF emission with a 266 nm excitation beam and the Rayleigh cross-section of helium is negligible compared with that of air. The LIF and Rayleigh scattering images of a flatfield, i.e. a uniform acetone-doped air flow field, were used for calibration of the system response (obtaining the constant of proportionality). Issues in using LIF, such as laser intensity attenuation due to absorption and quenching, are accounted for in the data reduction stage (Cai *et al.* 2011*b*).

Typically 7500–7800 images were used to obtain the SGS scalar statistics. Two components of scalar dissipation rates and diffusion were obtained with the scalar derivatives calculated using the 10th-order central difference schemes. Noise correction was performed for the root-mean-square (r.m.s.), correlation coefficient and conditionally filtered dissipation rates using the same method as Cai *et al.* (2011*b*). The conditional noise

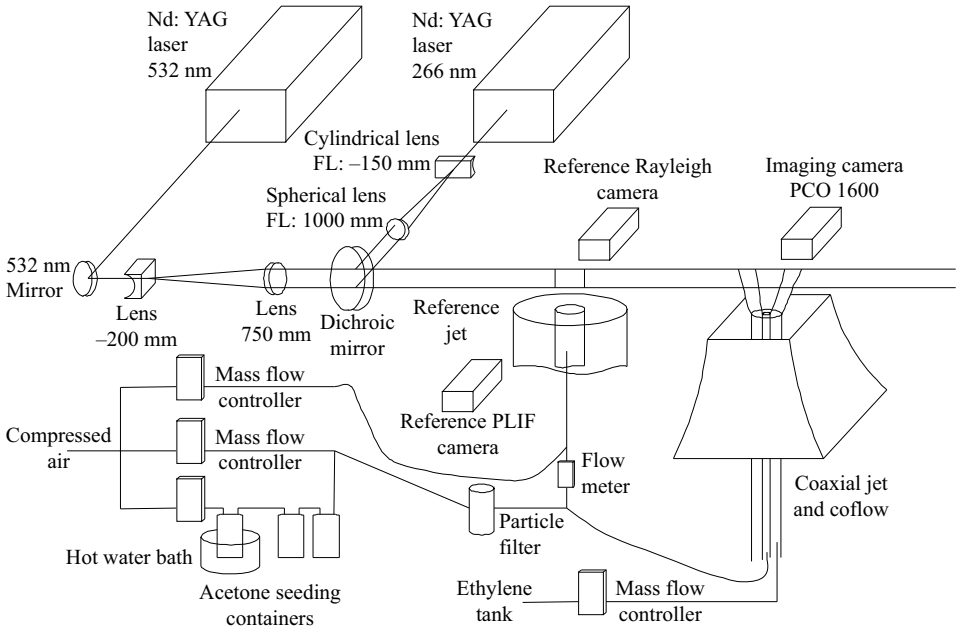

Figure 2. Schematic of the experimental set-up.

variances obtained experimentally were the same as in table 3 of Li *et al.* (2017). The f.j.d.f., conditionally filtered diffusion magnitudes and conditionally filtered dissipation rates were calculated using kernel density estimation (KDE) (Wand & Jones 1995) in two dimensions with a resolution of 400 by 400 in the scalar sample space with an oversmooth parameter of 1.3.

The statistical uncertainty and bias for the f.j.d.f. were estimated using the bootstrap method (Hall 1990). The r.m.s uncertainties of the f.j.d.f. were approximately 2–4 % near the f.j.d.f. peaks, and were less than 9 % near the contour for 90 % integrated probability, rising to 12 % near 99 % contour. The bias was typically less than 4 % for much of the sample space, and was less than 12 % at the 90 % contour, only rising to 16 % for the 99 % contour. The mean squared error was less than 5 %, 11 % and 20 %, respectively.

The statistical uncertainty and bias for the conditional dissipation rates and conditional diffusion magnitudes were estimated by the method given by Ruppert (1997). The r.m.s. uncertainties of both $\langle \chi_1 | \phi_1, \phi_2 \rangle_L$ and $\langle \chi_2 | \phi_1, \phi_2 \rangle_L$ were typically 2–4 % of the dissipation rates near the f.j.d.f. peaks, only rising to 8 % near the 90 % f.j.d.f. contour. The bias was typically less than 8 % for $\langle \chi_1 | \phi_1, \phi_2 \rangle_L$ and 5 % for $\langle \chi_2 | \phi_1, \phi_2 \rangle_L$, rising to 16 % and 13 % near the 90 % f.j.d.f. contour, respectively. The r.m.s. uncertainties of the conditional diffusion were approximately 2 % near the f.j.d.f. peaks and were less than 5 % near the 90 % f.j.d.f. contour, rising to 7 % near the 99 % f.j.d.f. contour. The bias of the conditional diffusion was typically less than 3 % for much of the sample space and was less than 9 % near the 90 % f.j.d.f. contour, only rising to 12 % near the 99 % f.j.d.f. contour.

3. Results

In this section the filtered scalar means, the filtered mean scalar SGS variances, the scalar f.j.d.f., the conditionally filtered scalar dissipation rates, conditionally filtered

cross-dissipation rate and the conditionally filtered diffusion are analysed to study the SGS mixing. We compute the means of these variables conditional on the filtered value and the SGS variance of ϕ_1, given as

$$\langle \phi_1 \rangle_L = \int \phi_1(\boldsymbol{x}') G(\boldsymbol{x} - \boldsymbol{x}')\, \mathrm{d}\boldsymbol{x}' \tag{3.1}$$

and

$$\langle \phi_1''^2 \rangle_L = \int \{\phi_1(\boldsymbol{x}') - \langle \phi_1 \rangle_L(\boldsymbol{x})\}^2 G(\boldsymbol{x} - \boldsymbol{x}')\, \mathrm{d}\boldsymbol{x}'. \tag{3.2}$$

In the present three-scalar mixing problem, ϕ_1 is analogous to the mixture fraction in a non-premixed reactive flow. Due to the important role of mixture fraction in such flows, previous studies (Cai *et al.* 2009, 2011*a*; Liu & Tong 2013) have obtained the conditionally filtered dissipation and diffusion using the filtered mixture fraction and the mixture fraction SGS variance as conditioning variables. Thus the conditioning variables in the present study ensure that the SGS mixing process approximates as closely as possible that in a non-premixed reactive flow. Typically 7200–7500 images were used to obtain the statistics. Several filter widths (Δ) ranging from 0.25 to 0.8 mm were used. To ensure that the results are relevant to LES at high Reynolds numbers, the filter widths employed must be in the inertial range (significantly larger than the dissipation scale, ∼0.014 mm Li *et al.* 2017), so that the subgrid scales contain sufficient fluctuations, as would LES of a high-Reynolds-number flow. Tong (2001) showed that a ratio between the two of larger than 30 is needed to ensure that the filter width is in the (inertial) scaling range, which is satisfied by $\Delta = 0.53$ and 0.8 mm. Given the moderate Reynolds number of the coaxial jet, the filter widths employed were not very small compared with the integral length scales. Nevertheless, they were preferable than smaller filter widths, which would be too close to the dissipative scales. The filter width of 0.53 mm is a good compromise between minimizing the filter width and being in the (inertial) scaling range. Furthermore, previous studies (e.g. Tong 2001; Wang & Tong 2002) have shown that when the filter width is much larger than the dissipation scales the properly scaled conditional statistics are not sensitive to the filter width. Thus, the results for the f.j.d.f. and the SGS mixing terms were only given for the 0.53 mm filter.

We note that Pope (2000) gave a criterion that LES should resolve 80 % of the turbulent kinetic energy. The criterion is aimed at ensuring that in actual LES the SGS stress and fluxes do not strongly affect the energy containing scales provided that the spectral energy transfer rate is correctly modelled. The objective of the present work is to investigate SGS mixing. Therefore, while for the filter width of 0.53 mm, the peak SGS variance is 20% of the peak scalar variance, meeting Pope's criterion, our overarching consideration is that the SGS scales have sufficient fluctuations to be representative of those in a high-Reynolds-number LES. The ratio of the filter width to the integral length scale may have some influence on the SGS scales. However, this influence is much weaker than that of the ratio of Δ to the dissipation length scale.

3.1. *SGS mixing on the jet centreline*

The profiles of the mean filtered scalars, $\langle \langle \phi_1 \rangle_L \rangle$ and $\langle \langle \phi_2 \rangle_L \rangle$, on the jet centreline for Case I are shown in figure 3. The difference in the mean filtered scalars between different filter scales were negligible. The mean filtered scalars were very close to the mean scalar profiles for the filter scales considered. The general trends were similar for other cases (figures not shown).

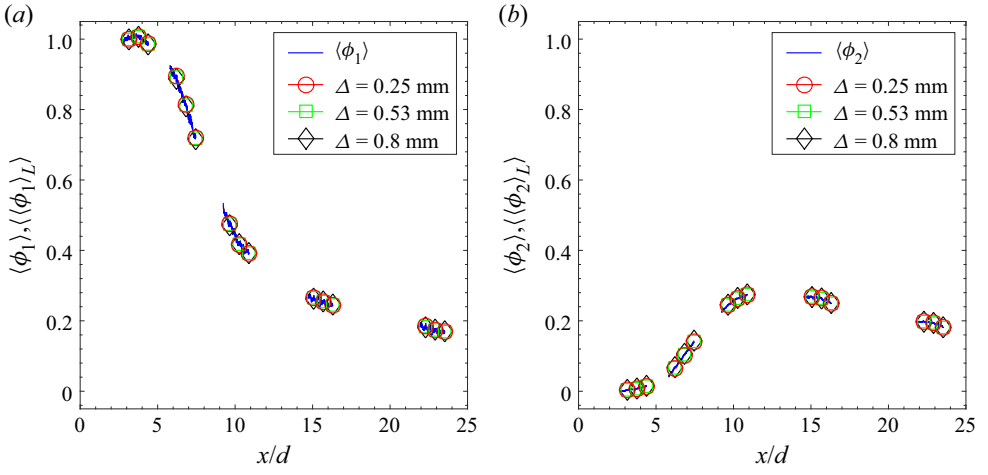

Figure 3. Centreline profiles of the filtered mean scalar for Case I.

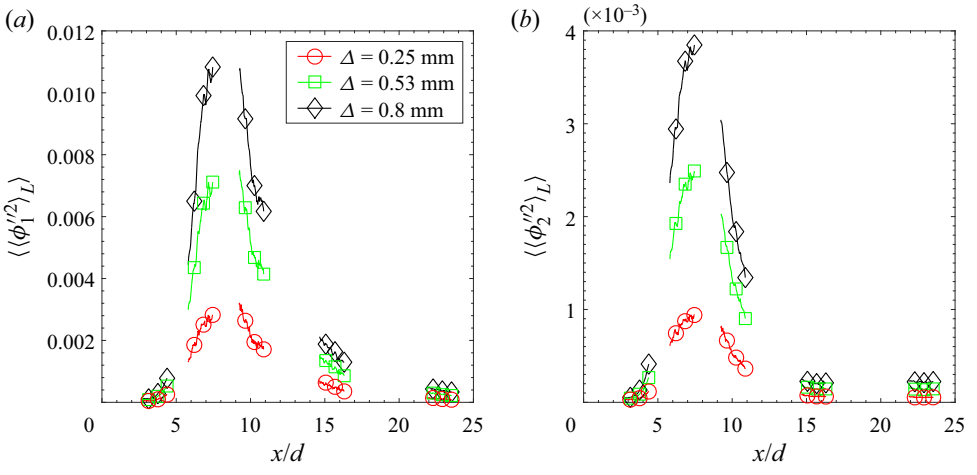

Figure 4. Centreline profiles of the filtered mean SGS variance for Case I.

The profiles of the mean SGS scalar variances, $\langle\langle\phi_1''^2\rangle_L\rangle$ and $\langle\langle\phi_2''^2\rangle_L\rangle$, on the jet centreline for Case I are shown in figure 4. The SGS scalar variances evolved similarly as the scalar variances. Their values, however, were significantly smaller than the scalar variances. The peak value of $\langle\langle\phi_1''^2\rangle_L\rangle$ was approximately 8 %, 20 % and 32 % of $\langle\phi_1'^2\rangle$ for the three filter widths ($\Delta = 0.25, 0.53, 0.8$ mm), respectively, while $\langle\langle\phi_2''^2\rangle_L\rangle$ is 6.5 %, 17 % and 27 % of $\langle\phi_2'^2\rangle$. The general trends were similar for the other cases (figures not shown). The relative magnitudes of the mean SGS variances among the cases were similar to those of the scalar variances (Li *et al.* 2017), with the peak values generally larger for cases with the higher velocity ratio and larger annulus width.

The results for the f.j.d.f. are given as a conditional mean, $\langle f|\langle\phi_1\rangle_L, \langle\phi_1''^2\rangle_L\rangle$, referred to simply as f.j.d.f. hereafter for convenience. The f.j.d.f. conditional on the small SGS variance on the centreline for Case I are shown in figure 5. The values of the conditional

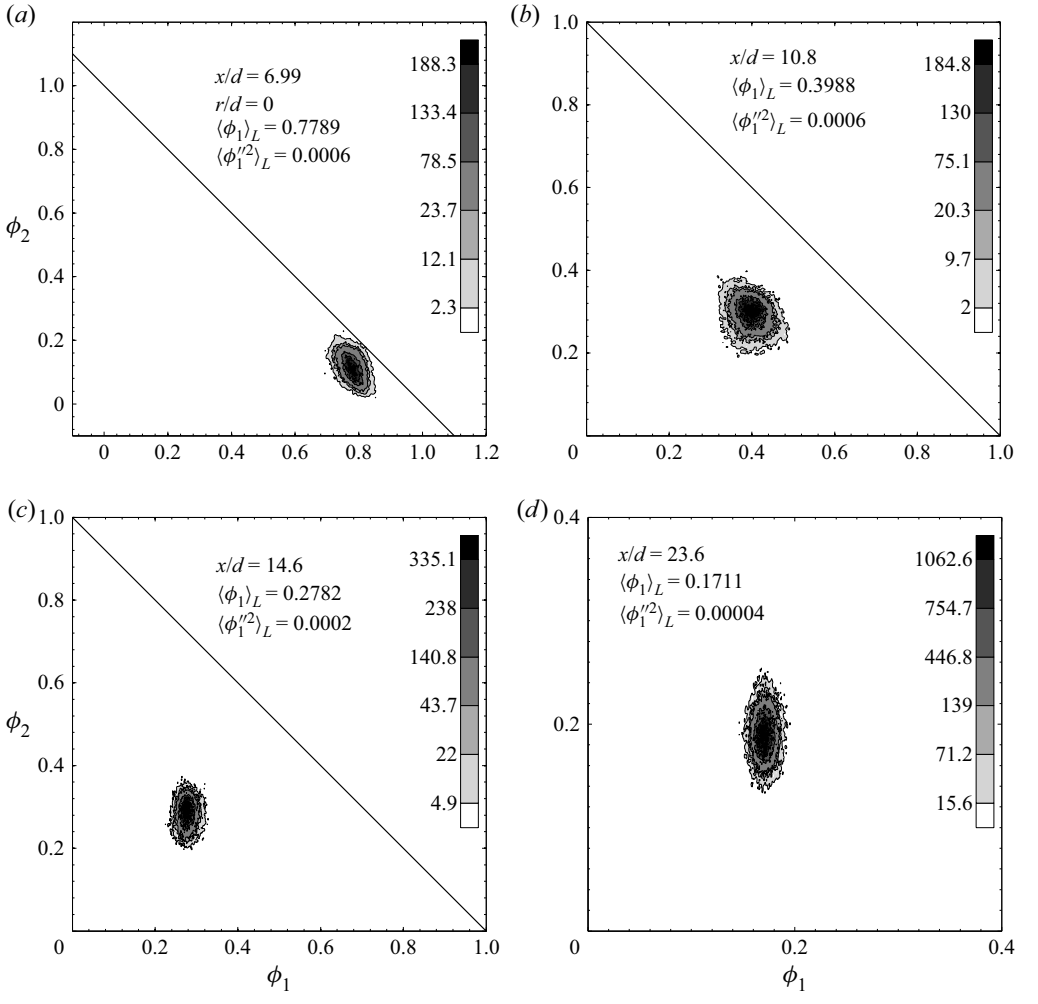

Figure 5. Evolution of the scalar f.j.d.f. conditional on the small SGS variance on the centreline for Case I. The last three contours correspond to boundaries within which the f.j.d.f. integrates to 90 %, 95 % and 99 %, respectively throughout the paper. The rest of the contours scale linearly over the remaining range. The filter width is 0.53 mm hereafter.

variables, $\langle\phi_1\rangle_L$ and $\langle\phi_1''^2\rangle_L$, are given in each figure. The value of $\langle\phi_1\rangle_L$ was chosen to be its local mean, $\langle\langle\phi_1\rangle_L\rangle$, at the physical location. We used greyscales and isocontours to represent the f.j.d.f. The outermost contour represents the boundary within which the f.j.d.f. integrates to 99 %. The f.j.d.f. should be confined to a triangle in the ϕ_1–ϕ_2 space with the vertices at (1, 0), (0, 1) and (0, 0), where the coordinates denote the sample-space variables for ϕ_1, ϕ_2 and ϕ_3, respectively. For small SGS variance, the f.j.d.f. was always unimodal and appeared to have a Gaussian-like shape. For $x/d < 5$ (for convenience we use d to denote the inner diameter of the inner tube D_{ji} in table 1), it was centred on the ϕ_1–ϕ_2 mixing line connecting (1, 0) and (0, 1), which indicated that the SGS scalars contained little co-flow air (not shown). Further downstream the f.j.d.f. moved away from the mixing line towards (0, 0) due to mixing with the co-flow air. The evolution of the peak

of the f.j.d.f. was generally consistent with filtered mean values. The general trends were similar for other cases (figures not shown).

For large SGS variance (generally more than four times the mean SGS variance), the f.j.d.f. close to the jet exit ($x/d < 8$) was unimodal (figure 6), with the peak near (1, 0) and a long tail. The area of the f.j.d.f. was much larger than for the small SGS variance, consistent with the relative magnitudes of the SGS variance. At $x/d = 10.8$, the f.j.d.f. became bimodal for both Cases I and II, which indicated that the SGS mixing was to a large extent between two distinct and segregated SGS mixtures. The two SGS scalars (ϕ_1'' and ϕ_2'') were negatively correlated at this location. At $x/d = 14.6$, the two peaks became closer and were further away from the mixing line due to the presence of more co-flow air. The ridgeline of the f.j.d.f. was horizontal for both cases with the f.j.d.f. of Case II having a more slender shape, consistent with better molecular mixing due to the existence of mean shear between the centre jet and the annular stream. Further downstream ($x/d = 23.6$), the f.j.d.f. was still bimodal while moving closer to (0, 0). The two peaks were also much closer with the SGS scalars becoming positively correlated, which indicated that they were well mixed, and that they were mixing largely in unison with the co-flow air.

These results were in contrast to the j.p.d.f. (for the smaller annulus cases), which was always unimodal on the centreline (Li *et al.* 2017). The different behaviours of the j.p.d.f. and f.j.d.f. were similar to those of the p.d.f. (unimodal) and f.d.f. (unimodal and bimodal) in binary mixing. Therefore, similar to the binary SGS mixing, there also existed two regimes for the three-scalar SGS mixing: for small SGS variance the SGS scalars were relatively well mixed, whereas for large SGS variance the SGS scalars were highly segregated.

The physics behind the two regimes is also likely to be similar to that of binary SGS mixing. Previous results (Tong 2001; Wang & Tong 2002) on binary SGS mixing have shown that for small SGS variance, the spectral transfer of the scalar variance is in equilibrium, i.e. the instantaneous spectral transfer rate of the scalar variance is comparable to or smaller than the instantaneous locally averaged scalar dissipation rate, whereas for large SGS variance, the SGS variance is in spectral non-equilibrium with the spectral transfer rate much larger. The bimodal f.j.d.f. observed here indicated that in three-scalar SGS mixing, spectral non-equilibrium also exists for large SGS variance, and is responsible for the bimodal f.j.d.f. Furthermore, there exists a ramp–cliff structure in the SGS scalar, ϕ_1'', which separates the two SGS mixtures. Bimodal f.j.m.d.f. of mixture fracture and temperature has also been observed in turbulent partially premixed flames (Wang *et al.* 2007*a*; Cai *et al.* 2009).

The loss of the initial three-scalar mixing configuration for small SGS variance suggested that for a SGS volume having the three-scalar mixing configuration, subsequent reduction of the SGS variance due to SGS mixing can destroy the configuration, rendering the SGS volume well mixed. The implication for a non-premixed turbulent flame is that the loss of the mixing configuration which generally corresponds to non-premixed flamelets, would imply destruction of such flamelets (Wang *et al.* 2007*a*). Our previous work using the data of the Sandia Flames (Wang *et al.* 2007*a*; Cai *et al.* 2009, 2011*a*) have shown that for small SGS variance, the SGS mixture fraction fluctuations are smaller than the reaction zone width in the mixture fraction space, based on 10 % of the peak CO oxidation reaction rate obtained in laminar flame calculations of Frank, Kaiser & Long (2002), i.e. there are turbulent fluctuations inside the reaction zones. These results further showed that for small SGS variance, the SGS mixture fraction, the scalar dissipation (Wang *et al.* 2007*a*;

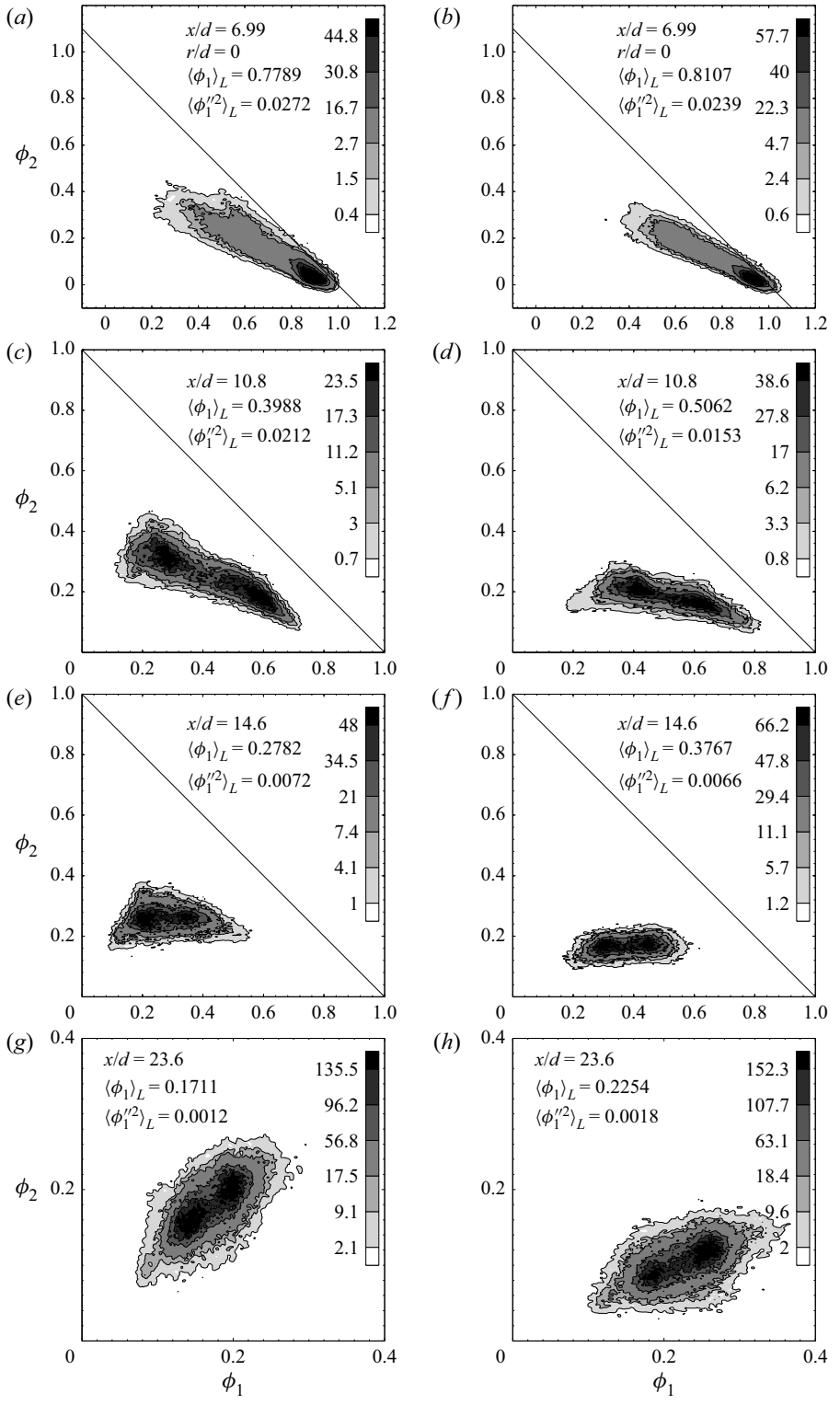

Figure 6. Evolution of the scalar f.j.d.f. conditional on the large SGS variance on the centreline for Case I (*a*,*c*,*e*,*g*) and Case II (*b*,*d*,*f*,*h*).

Cai *et al.* 2009), and the scalar and temperature diffusion (Cai *et al.* 2011*a*) in burning SGS flames, are consistent with the distributed reaction zones (Cai *et al.* 2009). Therefore, the loss of the mixing configuration also implies generation of such reaction zones in burning SGS fields. In SGS fields having small SGS variance and containing extinguished mixtures, the results imply that premixed flamelets and stratified reaction layers can exist, as suggested by the temperature dissipation (Cai *et al.* 2011*a*).

The general trends for larger annulus cases (figure 7) are generally similar to those of the smaller annulus. The f.j.d.f. extends further along the ϕ_1–ϕ_2 mixing line before bending towards (0, 0), which indicates slower progression of SGS mixing for the larger annulus cases. The f.j.d.f. is unimodal for Case III at $x/d = 10.9$ while it is bimodal for Case IV, in spite of the smaller value of the SGS variance chosen for the latter (because the mean SGS variance is smaller). This difference is in contrast to the j.p.d.f. on the centreline in that j.p.d.f. is bimodal at some locations for Case III but is always unimodal for Case IV (Li *et al.* 2017). Moving downstream ($x/d = 14.6$), the f.j.d.f. also becomes bimodal for Case III. Similar to the smaller annulus cases, the f.j.d.f. is bimodal for both cases further downstream ($x/d = 23.6$) and the two SGS scalars are positively correlated. These results show that similar to binary SGS mixing (Tong 2001; Wang & Tong 2002), the f.j.d.f. can be bimodal even when the j.p.d.f. is unimodal everywhere (Cases II and IV). The earlier appearance of the bimodal f.j.d.f. for Case IV is likely due to the stronger SGS transport resulting from the SGS velocity and scalar fluctuation generated by the mean shear between the centre stream and the annular stream and between the annular stream and the co-flow.

3.2. *Cross-stream SGS profiles*

The radial profiles of the mean SGS variances are shown in figure 8. They have similar shapes and peak locations to the scalar variances (Li *et al.* 2017). Similar to the variance of ϕ_1, the peak location of $\langle\langle\phi_1''^2\rangle_L\rangle$ moves towards the centreline as x/d increases. The peak value of $\langle\langle\phi_1''^2\rangle_L\rangle$ decreases as x/d increases for all cases, whereas the peak value of ϕ_1 variance for Case III increases from $x/d = 3.29$ to $x/d = 6.99$. This difference is likely because the scalar integral length scale increases with x/d; for a fixed filter width, the fraction of the variance contained in the SGS decreases. The mean SGS variance of ϕ_2 also have the same trend as the variance of ϕ_2. The peak values decrease with increasing x/d. The mean SGS variance, however, decreases faster than the variance due to the increasing integral length scale. The relative magnitudes of the mean SGS variances among the cases are also similar to those of scalar variances. The peak values of both ϕ_1 and ϕ_2 mean SGS variances are smaller and decrease faster for Case II (IV) than for Case I (III). However, the profiles of $\langle\langle\phi_1''^2\rangle_L\rangle$ are wider for Case II (IV) than for Case I (III). The peak values are generally smaller and decrease faster for the smaller annulus cases than for the larger annulus cases, except that the peak value of $\langle\langle\phi_1''^2\rangle_L\rangle$ at $x/d = 3.29$ is larger for Case I than for Case III. The general trends for the other filter width are similar but with different magnitudes.

The SGS correlation coefficient between ϕ_1 and ϕ_2,

$$\rho = \frac{\langle\langle\phi_1''\phi_2''\rangle_L\rangle}{\langle\langle\phi_1''^2\rangle_L\rangle^{1/2}\langle\langle\phi_1''^2\rangle_L\rangle^{1/2}}, \tag{3.3}$$

is shown in figure 9. The correlation coefficient generally has the value of negative one close to the centreline, increasing towards unity far away from the centreline. Close to the centreline, ϕ_1'' and ϕ_2'' are anticorrelated ($\rho \approx -1$) because there is virtually no ϕ_3.

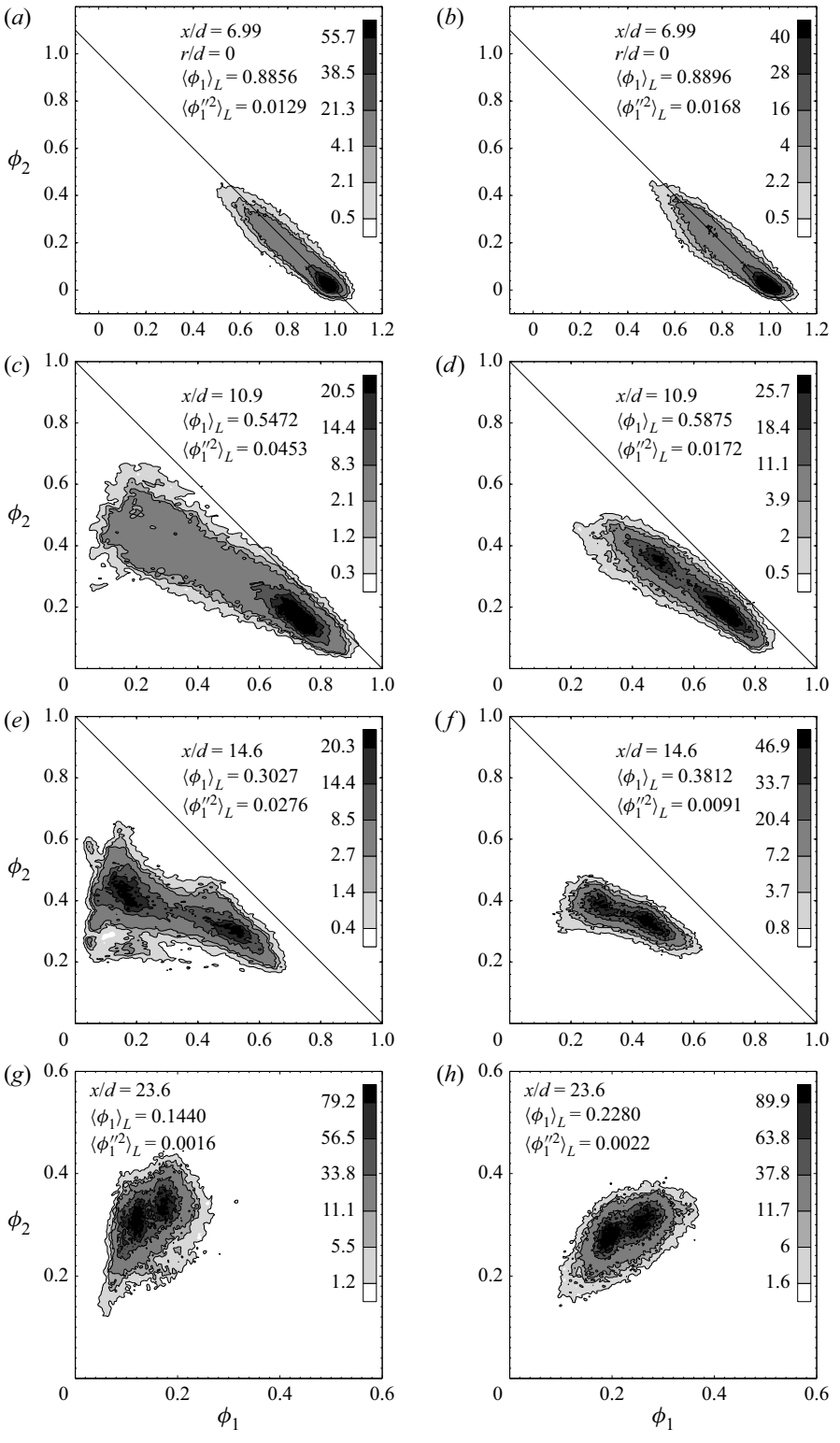

Figure 7. Evolution of the scalar f.j.d.f. conditional on the large SGS variance on the centreline for Case III (*a*,*c*,*e*,*g*) and Case IV (*b*,*d*,*f*,*h*).

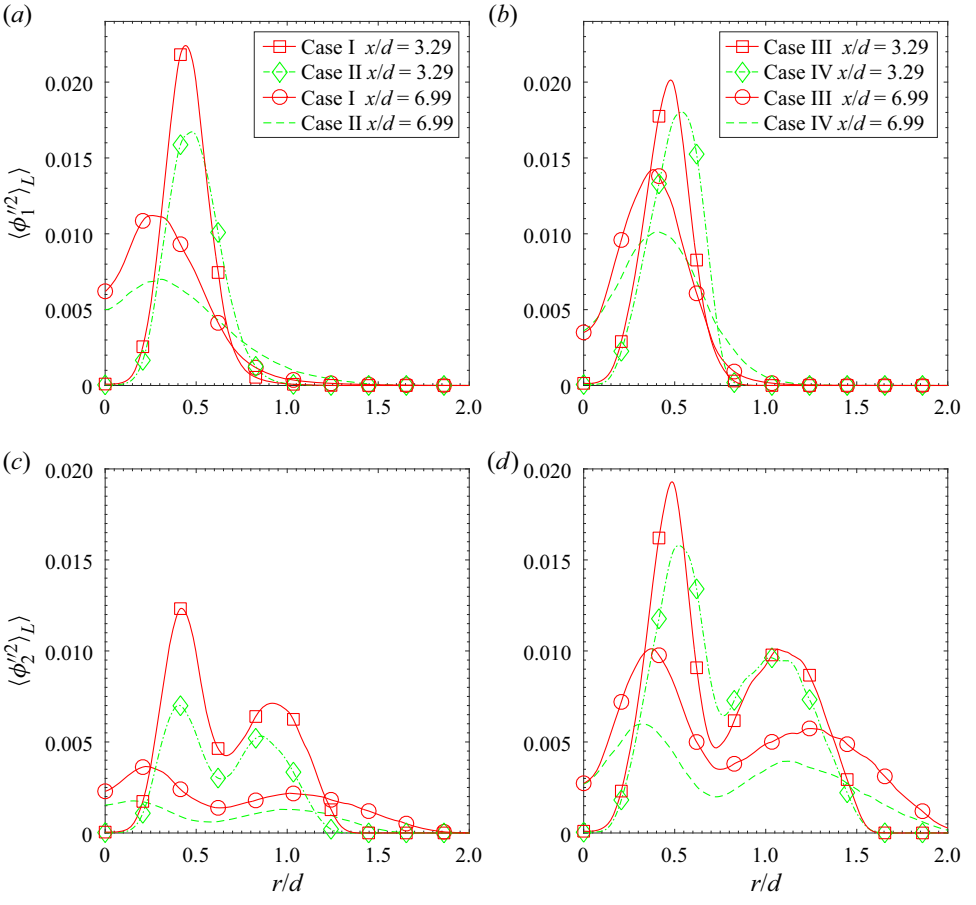

Figure 8. Cross-stream filtered mean SGS variance profiles.

It begins to increase when ϕ_1 and ϕ_2 begin to mix with ϕ_3, and approaches unity far away from the centreline, which indicates that the two SGS scalars are well mixed and are in phase. The correlation at $x/d = 6.99$ begins to dip at approximately $r/d = 1.8$, due to residual measurement noise, i.e. after noise correction. At $x/d = 3.29$, the results for both close to the centreline and towards the edge of the jet (at approximately $r/d = 1$) are not shown, because the scalar fluctuations are small and the measured correlation coefficient is dominated by the residual measurement noise. The correlation coefficient begins to increase at smaller r/d values at $x/d = 6.99$ than at $x/d = 3.29$, which results from the progression of scalar mixing. The differences between Cases I and II and between Cases III and IV are small. Comparisons between Cases I and III and between Cases II and IV show that the evolution of the correlation coefficient is much slower for the larger annulus than for the smaller annulus.

3.3. *Cross-stream f.j.d.f. and conditionally filtered diffusion*

In this section we discuss the f.j.d.f. and the conditionally filtered diffusion at several radial locations in the near field ($x/d = 3.29$ and 6.99). The conditionally filtered diffusion is given as conditional means, $\langle\langle D_1\nabla^2\phi_1|\hat{\phi}_1, \hat{\phi}_2\rangle_L|\langle\phi_1\rangle_L, \langle\phi_1''^2\rangle_L\rangle$ and $\langle\langle D_2\nabla^2\phi_2|\hat{\phi}_1, \hat{\phi}_2\rangle_L|\langle\phi_1\rangle_L, \langle\phi_1''^2\rangle_L\rangle$. The conditionally filtered scalar diffusion terms in the

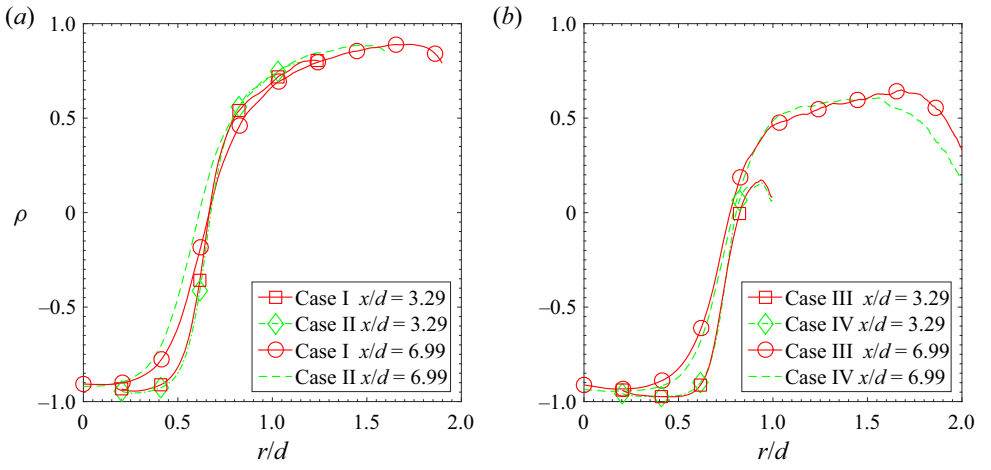

Figure 9. Cross-stream SGS correlation coefficient between ϕ_1 and ϕ_2.

f.j.d.f. equation transport the f.j.d.f. in the scalar space; therefore, the conditionally filtered diffusion represents the two components of a diffusion (or transport) velocity in the scalar space. We present the conditionally filtered diffusion as the diffusion velocity, represented by streamlines and magnitude isocontours in the same way that conditional diffusion was represented (Cai *et al.* 2011*b*; Li *et al.* 2017). Both conditionally filtered diffusion terms are non-dimensionalized by the square root of ϕ_1 SGS variance and the conditionally filtered dissipation time scale for ϕ_1'', $\langle\phi_1''^2\rangle_L/\langle\langle\chi_1\rangle_L|\langle\phi_1\rangle_L, \langle\phi_1''^2\rangle_L\rangle$.

At $x/d = 3.29$, close to the jet centreline (not shown) the f.j.d.f. is largely limited to the ϕ_1–ϕ_2 mixing line. The spread of the measured f.j.d.f. is largely due to the measurement uncertainties. For small SGS variance at $r/d = 0.372$ (figure 10), the f.j.d.f. is unimodal with the peak near the ϕ_1–ϕ_2 mixing line. The diffusion streamlines converge to the peak of the f.j.d.f. At $r/d = 0.496$, the f.j.d.f. still has a Gaussian-like shape but the peak has already moved away from the ϕ_1–ϕ_2 mixing line, which indicates that ϕ_1'' and ϕ_2'' are well mixed and there is some co-flow air present. The diffusion streamlines again converge to the stagnation point near $(\langle\phi_1\rangle_L, \langle\langle\phi_2\rangle_L|\langle\phi_1\rangle_L, \langle\phi_1''^2\rangle_L\rangle)$, which is also the peak of f.j.d.f. Further away from the centreline (at $r/d = 0.703$), the peak of the f.j.d.f. moves closer to (0, 0), consistent with the evolution of the filtered mean values. The general trends for other cases are also similar (figures not shown).

For large SGS variance, the f.j.d.f. close to the centreline (not shown) is concentrated at (1, 0) with a tail extending toward (0, 1), which indicates that the SGS mixing is largely limited to between ϕ_1 and ϕ_2 but with only a small amount of ϕ_3. At $r/d = 0.372$ (figure 11), the f.j.d.f. begins to extend toward (0, 0) for both Cases I and II. A diffusion manifold begins to emerge, and the diffusion streamlines converge to a stagnation point that is different from both the local filtered mean scalars and the peak of f.j.d.f. For Case II, it appears that a second peak begins to emerge on the left-hand side of the f.j.d.f. At $r/d = 0.496$ (figure 12), the f.j.d.f. has become bimodal for both cases with stronger bimodality for Case I, consistent with the larger SGS variance. The right peak is close to the ϕ_1–ϕ_2 mixing line without much ϕ_3, while the left peak contains little ϕ_1, which indicates that within the SGS field the two mixtures coming from the two mixing layers are segregated with a sharp interface (ramp–cliff) between them. The two SGS scalars are negatively correlated. The diffusion streamlines first move towards a well-defined and bell-shaped manifold, then continue along it to a stagnation point, which is again different from the filtered

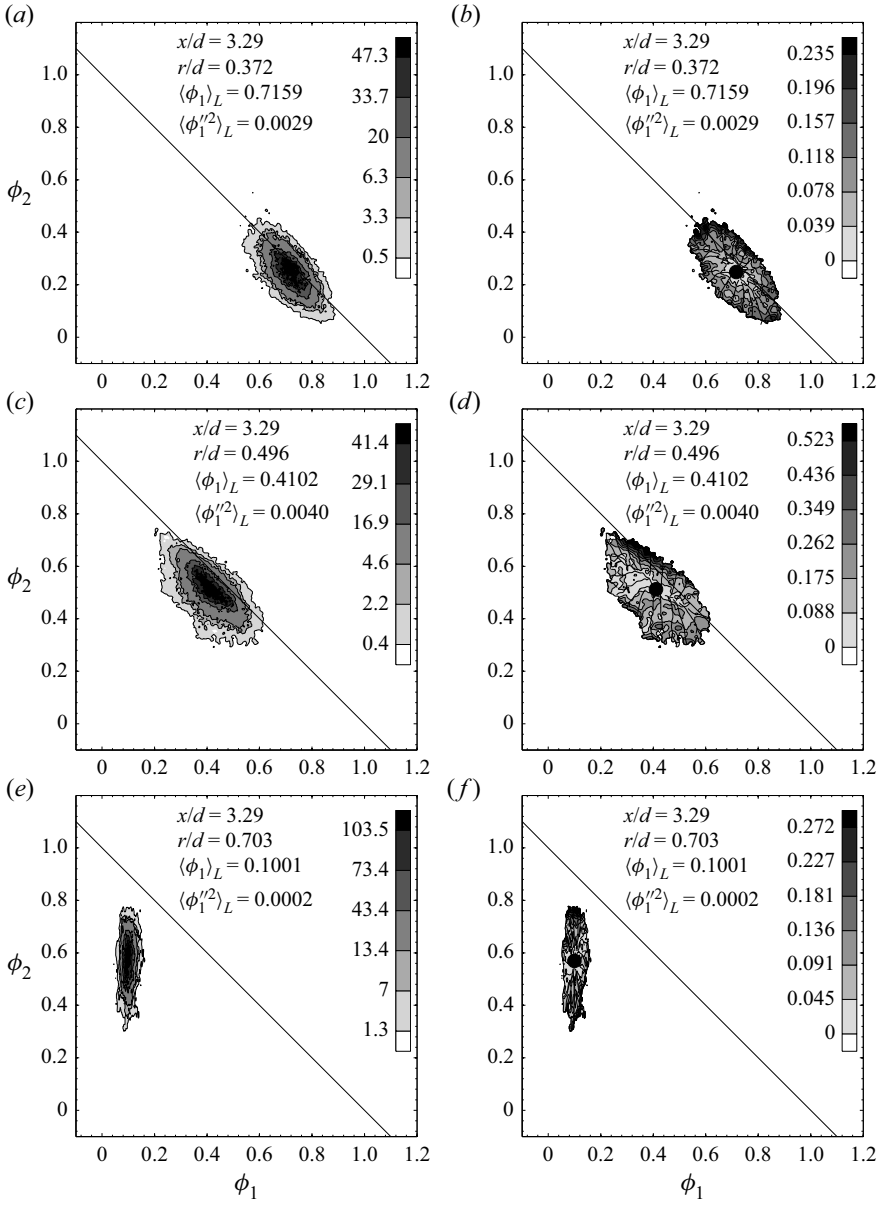

Figure 10. The f.j.d.f. (*a*,*c*,*e*) and conditionally filtered diffusion streamlines (*b*,*d*,*f*) conditional on the small SGS variance at $x/d = 3.29$ for Case I. The filtered scalar values ($\langle\phi_1\rangle_L$, $\langle\langle\phi_2\rangle_L|\langle\phi_1\rangle_L$, $\langle\phi_1''^2\rangle_L$) are denoted by a bullet in the streamline figures.

mean composition. Thus, the SGS scalars for large SGS variance have a structure due to the mixing configuration of the coaxial jet, whereas for small SGS variance the three scalars are quite well mixed and the configuration is lost. The curvature of the manifold appears to be larger for Case I than for Case II.

Further away from the centreline, the right peak of the f.j.d.f. becomes weaker. At $r/d = 0.703$ (figure 13), the right peak completely disappears for Case I whereas a weak right peak still exists for Case II, which indicates that the bimodal f.j.d.f. exists over a

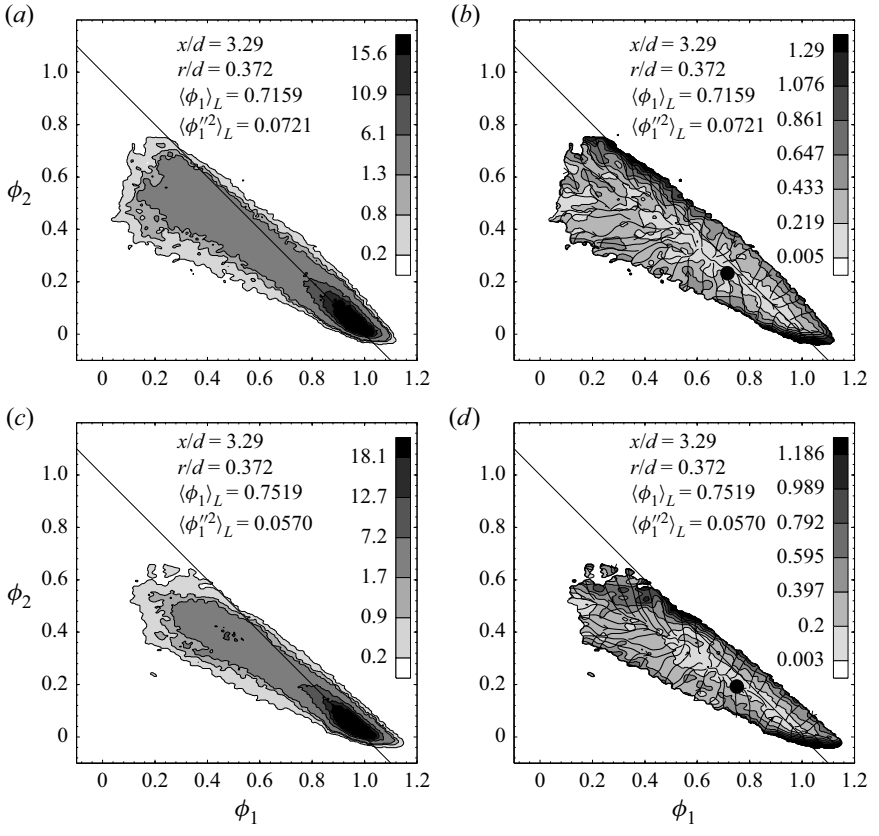

Figure 11. The f.j.d.f. (*a*,*c*) and conditionally filtered diffusion streamlines (*b*,*d*) conditional on the large SGS variance at $x/d = 3.29$ and $r/d = 0.372$ for Case I (*a*,*b*) and Case II (*c*,*d*).

wider range of physical locations for Case II. This trend is different from the cross-stream evolution of j.p.d.f. (Li *et al.* 2017), which is bimodal at some locations for Case I whereas it is always unimodal for Case II. (This difference will be further discussed in detail along with the results at $x/d = 6.99$.) The left peak of the f.j.d.f. has already moved very close to (0, 0). The streamlines converge directly to a stagnation point from larger ϕ_1 values (from the right), but appear to move to a manifold first from smaller ϕ_1 values (from the left) and then approach the stagnation point. The f.j.d.f. also becomes unimodal for Case II further away from the centreline.

Moving downstream to $x/d = 6.99$, some co-flow air has reached the centreline (Li *et al.* 2017). For small SGS variance, the conditional f.j.d.f. (not shown) again has a Gaussian-like shape and is concentrated near the filtered mean scalar values. The conditionally filtered diffusion streamlines (also not shown) mostly converge to a stagnation point. The trends of the f.j.d.f. and the diffusion streamlines with increasing r/d values are similar to those at $x/d = 3.29$. The f.j.d.f. and the conditionally filtered diffusion again indicate that the SGS scalars are relatively well mixed.

For large SGS variance, as shown in figure 6, the f.j.d.f. on the jet centreline is still concentrated near (1, 0), but extends further away from it, which indicates the penetration of both ϕ_2 and ϕ_3. Moving away from the centreline, the f.j.d.f. extends further towards lower ϕ_1 values and bends further towards (0, 0). A second peak begins to emerge and the

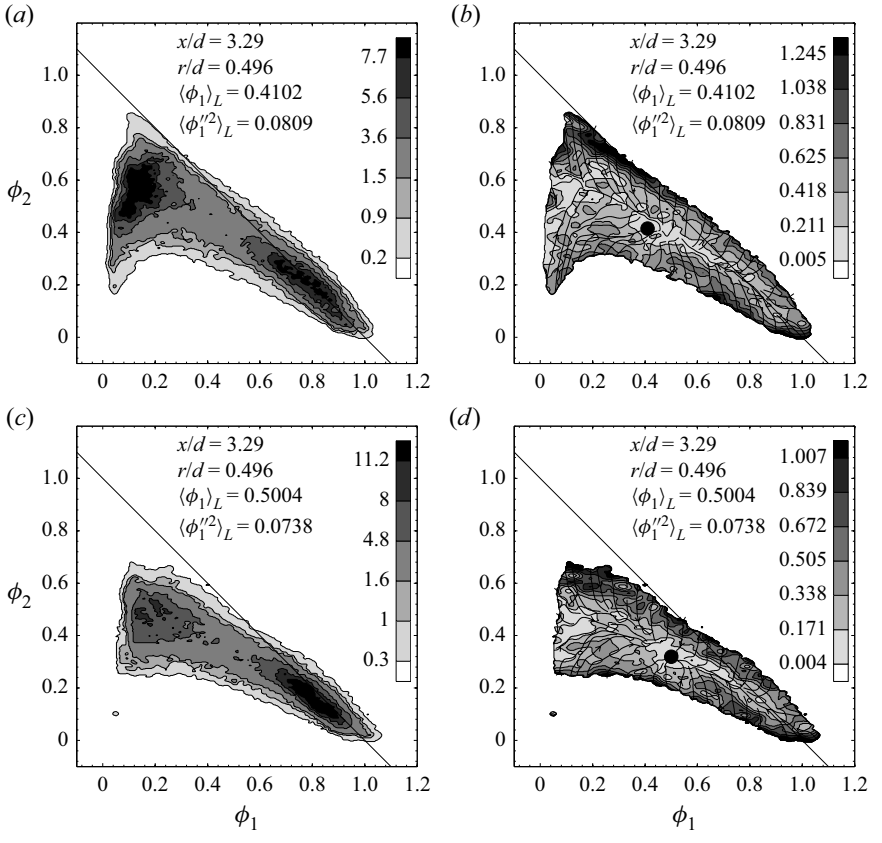

Figure 12. The f.j.d.f. (*a*,*c*) and conditionally filtered diffusion streamlines (*b*,*d*) conditional on the large SGS variance at $x/d = 3.29$ and $r/d = 0.496$ for Case I (*a*,*b*) and Case II (*c*,*d*).

f.j.d.f. becomes bimodal at $r/d = 0.248$ and $r/d = 0.207$ for Case I and Case II (figures not shown), respectively. At $r/d = 0.376$ (figure 14), similar to $x/d = 3.29$, the f.j.d.f. is strongly bimodal for both Cases I and II with the left peak further away from the mixing line, which indicates that the SGS field contains predominately the ϕ_1–ϕ_2 mixture and the ϕ_1–ϕ_2–ϕ_3 mixture coming from the two mixing layers. Again the mixtures are segregated with a cliff between them. Similar to $x/d = 3.29$, the diffusion streamlines first converge to a manifold, and then continue on the manifold at a lower rate towards a stagnation point. At $r/d = 0.538$ (figure 15), the f.j.d.f. becomes unimodal for Case I whereas it is still bimodal for Case II, although the SGS variance is again smaller for Case II. There is also a well-defined curved manifold for the conditional diffusion for each case. Towards the edge of the jet ($r/d = 0.827$), the f.j.d.f. is still bimodal for Case II but with ϕ_1'' and ϕ_2'' positively correlated (figure 16). For Case I, the diffusion streamlines to the left of the stagnation point converge to a manifold and then to the stagnation point, whereas those to the right converge to the stagnation point. For Case II, the curved manifold is better defined. Moving further away from the centreline, the f.j.d.f. is also unimodal for Case II (not shown).

For the larger annulus at $x/d = 3.29$ (figure 17), the general trends are similar to the smaller annulus cases. The main difference is that the peak of the f.j.d.f. evolves along the ϕ_1–ϕ_2 mixing line and reaches (0, 1) before bending towards (0, 0). At $r/d = 0.331$, the

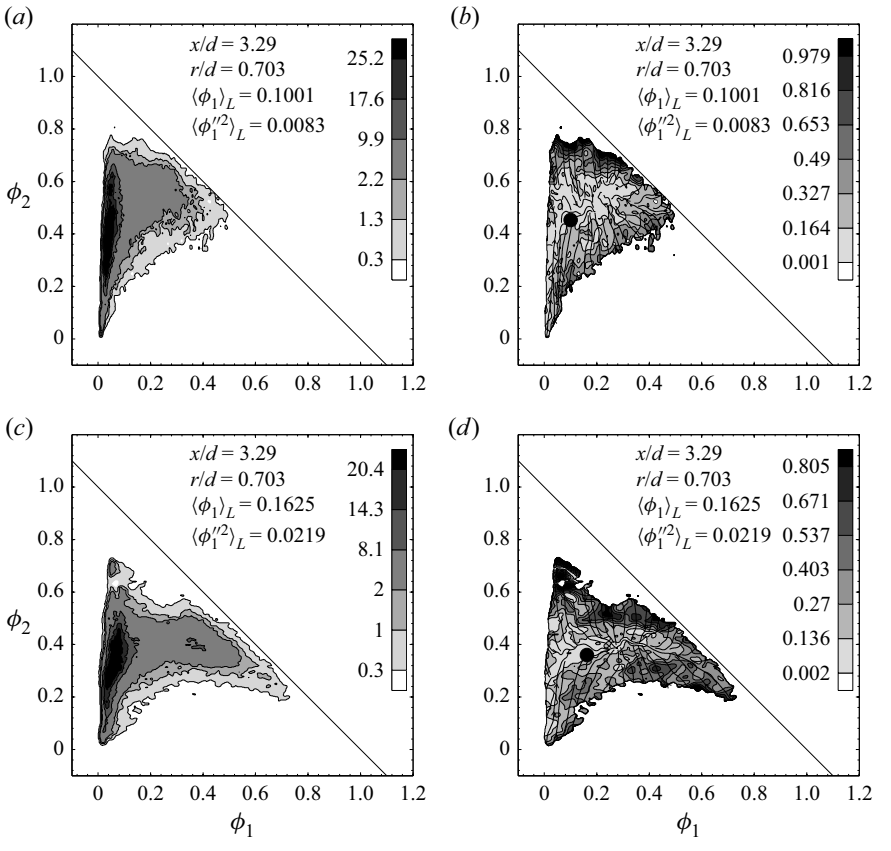

Figure 13. The f.j.d.f. (*a*,*c*) and conditionally filtered diffusion streamlines (*b*,*d*) conditional on the large SGS variance at $x/d = 3.29$ and $r/d = 0.703$ for Case I (*a*,*b*) and Case II (*c*,*d*).

f.j.d.f. peaks near (1, 0) while the ridgeline stays on the ϕ_1–ϕ_2 mixing line. A second peak begins to emerge on the left for Case IV. It is strongly bimodal for both Cases III and IV at $r/d = 0.488$. The f.j.d.f. is nearly symmetric with respect to the ϕ_1–ϕ_2 mixing line for Case III whereas it extends towards (0, 0) on the left for Case IV. The right peak disappears for Case III at $r/d = 0.62$ whereas a weak right peak still exists for Case IV. The peak near (0, 1) indicates that ϕ_1 and ϕ_3 are separated by pure ϕ_2, and there are two separate mostly binary mixing processes. A diffusion manifold begins to emerge for Case IV at $r/d = 0.62$ (figure 18), whereas there is no sign of a curved manifold for Case III. The f.j.d.f. would also become unimodal for Case IV moving further away from the centreline.

For the larger annulus at $x/d = 6.99$ (figures 19–21), the general trends are again similar to the smaller annulus cases. The bimodal f.j.d.f. exists over a wider range of physical locations for Case IV than for Case III, again a trend different from that of the j.p.d.f. The curvature of the diffusion manifold is also larger for Case III than for Case IV, consistent with better mixing for Case IV.

The above results show that the strongest bimodal f.j.d.f. occurs in Cases I and III at physical locations near the peaks of the mean SGS variance of ϕ_1. These cases have higher peak mean SGS variance values than Cases II and IV. The strongest bimodal j.p.d.f. also occurs (in Cases I and III, which have higher peak scalar variance values) near the peaks of the variance of ϕ_1 (Li *et al.* 2017). Therefore, a higher variance (as well as mean

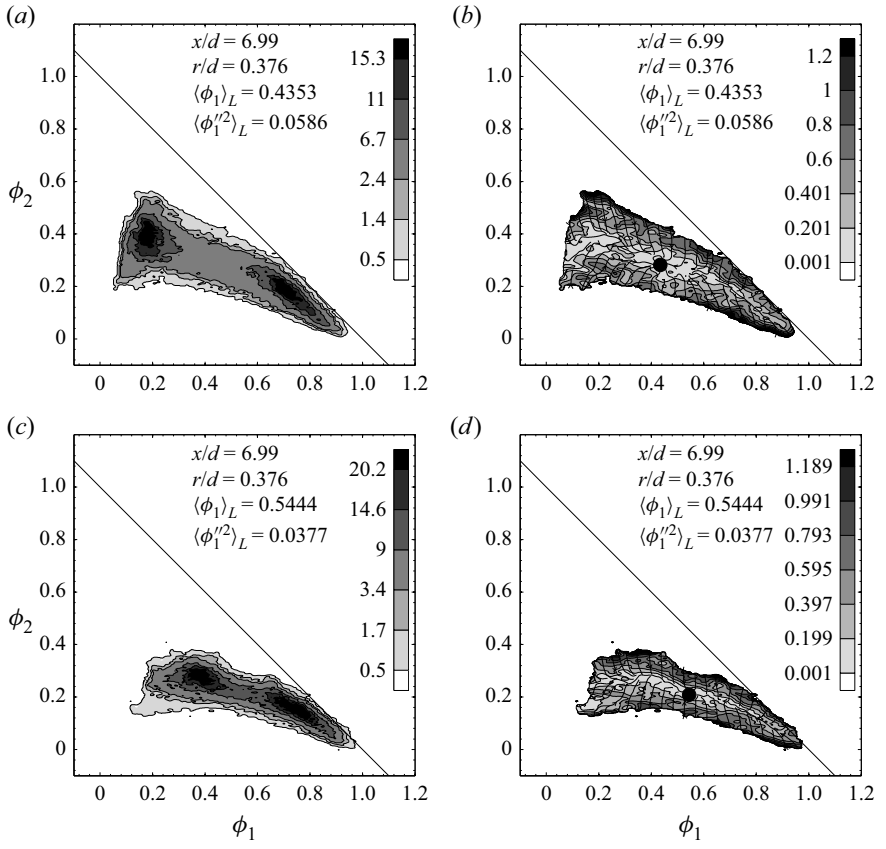

Figure 14. The f.j.d.f. (*a*,*c*) and conditionally filtered diffusion streamlines (*b*,*d*) conditional on the large SGS variance at $x/d = 6.99$ and $r/d = 0.376$ for Case I (*a*,*b*) and Case II (*c*,*d*).

SGS variance) is conducive to a bimodal j.p.d.f. (f.j.d.f.). On the other hand, the f.j.d.f. is bimodal over a wider range of physical locations for Cases II and IV than for Cases I and III, in spite of the weaker bimodality at the location of the peak mean SGS variance. Furthermore, while Cases II and IV have wider SGS variance profiles with higher values towards the edge of the jets than Cases I and III, thereby favouring bimodal f.j.d.f., there are also instances (e.g. at $x/d = 3.29$ and $r/d = 0.372$ for the smaller annulus shown in figure 11, and at $x/d = 3.29$ and $r/d = 0.331$ for the larger annulus shown in figure 17) where the f.j.d.f. is unimodal for Case I (larger mean SGS variance) and is bimodal for Case II (relatively smaller SGS variance). Therefore, a large SGS variance and the non-equilibrium spectral transfer is only one important factor determining the bimodality of the f.j.d.f. The other important factor is the length scales of the turbulent fluctuations, which influence the SGS scalar structure. Cases II and IV have two shear layers; therefore, the length scales of the turbulent (both velocity and scalar) fluctuations are smaller than those of Cases I and III, which have a single shear layer. Therefore, for a fixed filter width and SGS variance value, which correspond to a fixed ratio of the filter width to the centre jet length scale, the largest SGS scales for Cases II and IV, which have a larger length scale ratio between the annulus and the centre jet, have a stronger influence on the SGS structure, and are more likely to result in a bimodal f.j.d.f.

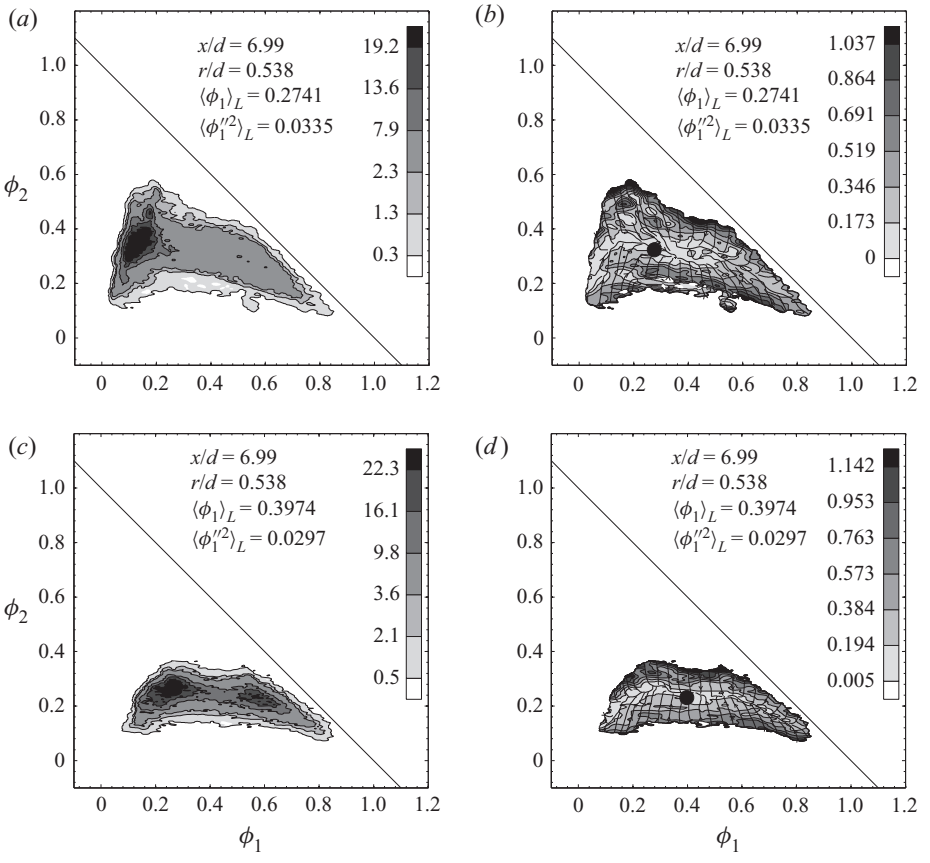

Figure 15. The f.j.d.f. (*a*,*c*) and conditionally filtered diffusion streamlines (*b*,*d*) conditional on the large SGS variance at $x/d = 6.99$ and $r/d = 0.538$ for Case I (*a*,*b*) and Case II (*c*,*d*).

Similar to the conditional diffusion for the j.p.d.f., for large SGS variance the diffusion streamlines first converge to a manifold and then continue along it towards a stagnation point. Thus, there are also two mixing processes in the SGS mixing, one slow and one fast. This phenomenon is related to the structure of the SGS scalars, in which ϕ_1 is dominated by a ramp–cliff structure (Tong 2001; Wang & Tong 2002) and ϕ_2 by a Gaussian-like scalar profile, both large-scale structures. The ramp–cliff structure is generated by a large-scale convergent–divergent separatrix (Holzer & Siggia 1994; Tong & Warhaft 1994) acting on a mean (or large-scale) scalar gradient. The large-scale scalar structures in ϕ_2 are also likely due to the same reason. Smaller scalar fluctuations may be viewed as being superimposed on these structures. These fluctuations are likely due to mixing of small-scale (somewhat homogeneous) scalar fields by velocity fluctuations of smaller scales. Consequently, the SGS scalars diffuse (relax) towards the largest SGS structures first before the diffusion of these structures move the streamlines towards the stagnation point. Thus, the slow and fast processes in SGS mixing are likely the results of large- and small-scale velocity fluctuations acting on large- and small-scale scalar gradients, respectively. The large-scale scalar structures also form a mixing path in the scalar space along which mixing of ϕ_1 and ϕ_3 occurs.

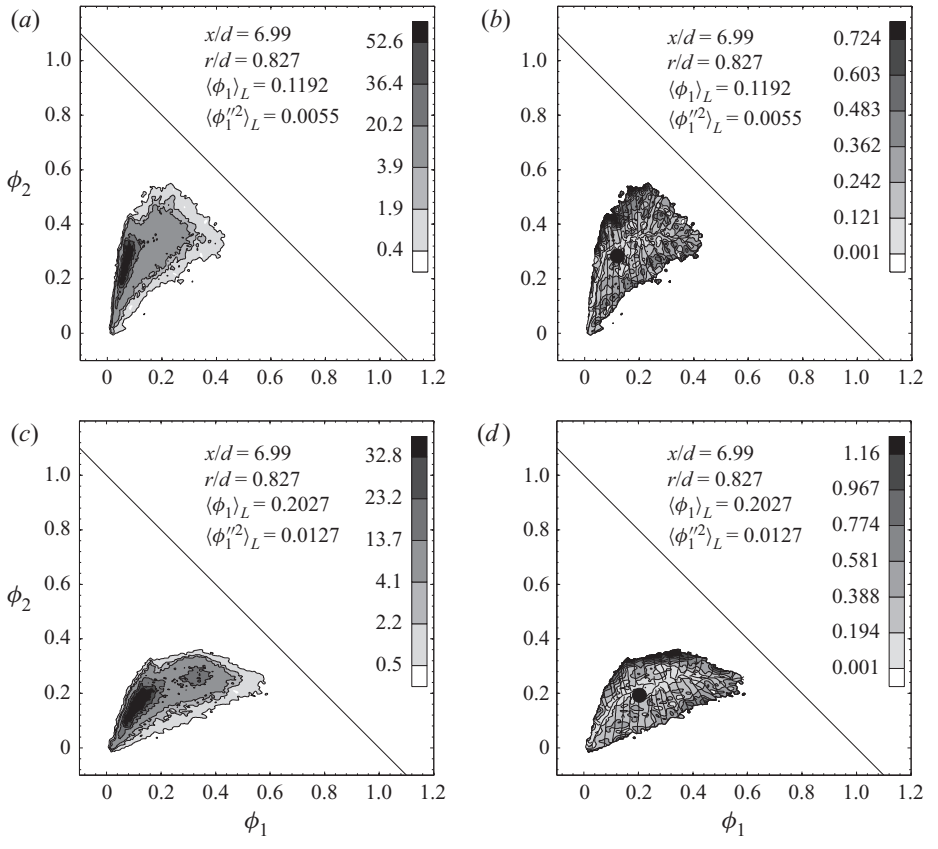

Figure 16. The f.j.d.f. (*a*,*c*) and conditionally filtered diffusion streamlines (*b*,*d*) conditional on the large SGS variance at $x/d = 6.99$ and $r/d = 0.827$ for Case I (*a*,*b*) and Case II (*c*,*d*).

3.4. *Conditionally filtered dissipation and cross-dissipation*

In this section we discuss the conditionally filtered dissipation, which are also given as conditional means, $\langle\langle\chi_i|\hat{\phi}_1, \hat{\phi}_2\rangle_L|\langle\phi_1\rangle_L, \langle\phi_1''^2\rangle_L\rangle$ and $\langle\langle\chi_{12}|\hat{\phi}_1, \hat{\phi}_2\rangle_L|\langle\phi_1\rangle_L, \langle\phi_1''^2\rangle_L\rangle$. For convenience, the conditionally filtered dissipation and cross-dissipation are referred to as $\langle\chi_i|\phi_1, \phi_2\rangle_L$ and $\langle\chi_{12}|\phi_1, \phi_2\rangle_L$ hereafter. The conditionally filtered dissipation rates are non-dimensionalized by the maximum ϕ_1 mean dissipation rate at the same x/d location.

For small SGS variance, the conditionally filtered conditional dissipation rates for ϕ_1 and ϕ_2 share a similar pattern close to the centreline for Cases I and II (not shown). The dissipation rates are small close to (1, 0) and increase towards (0, 1). These similarities are because there is essentially no co-flow air at this location and the SGS mixing is only between ϕ_1 and ϕ_2. Thus, their fluctuations have equal magnitudes but are anticorrelated, which results in similar dissipation rates. The cross-dissipation is also similar but has negative values due to the anticorrelation. For Case I at $r/d = 0.372$ (figure 22), both $\langle\chi_1|\phi_1, \phi_2\rangle_L$ and $\langle\chi_2|\phi_1, \phi_2\rangle_L$ as well as $\langle\chi_{12}|\phi_1, \phi_2\rangle_L$ are relatively uniform, consistent with the Gaussian-like f.j.d.f. since the SGS scalars are well mixed for small SGS variance. The cross-dissipation still has the same trend as $\langle\chi_1|\phi_1, \phi_2\rangle_L$ and $\langle\chi_2|\phi_1, \phi_2\rangle_L$, but with negative values due to the mixing being primarily between ϕ_1 and ϕ_2. The magnitudes are between those of $\langle\chi_1|\phi_1, \phi_2\rangle_L$ and $\langle\chi_2|\phi_1, \phi_2\rangle_L$. Moving towards the edge of the jet (figures not shown), the general trends are opposite to those close to the centreline,

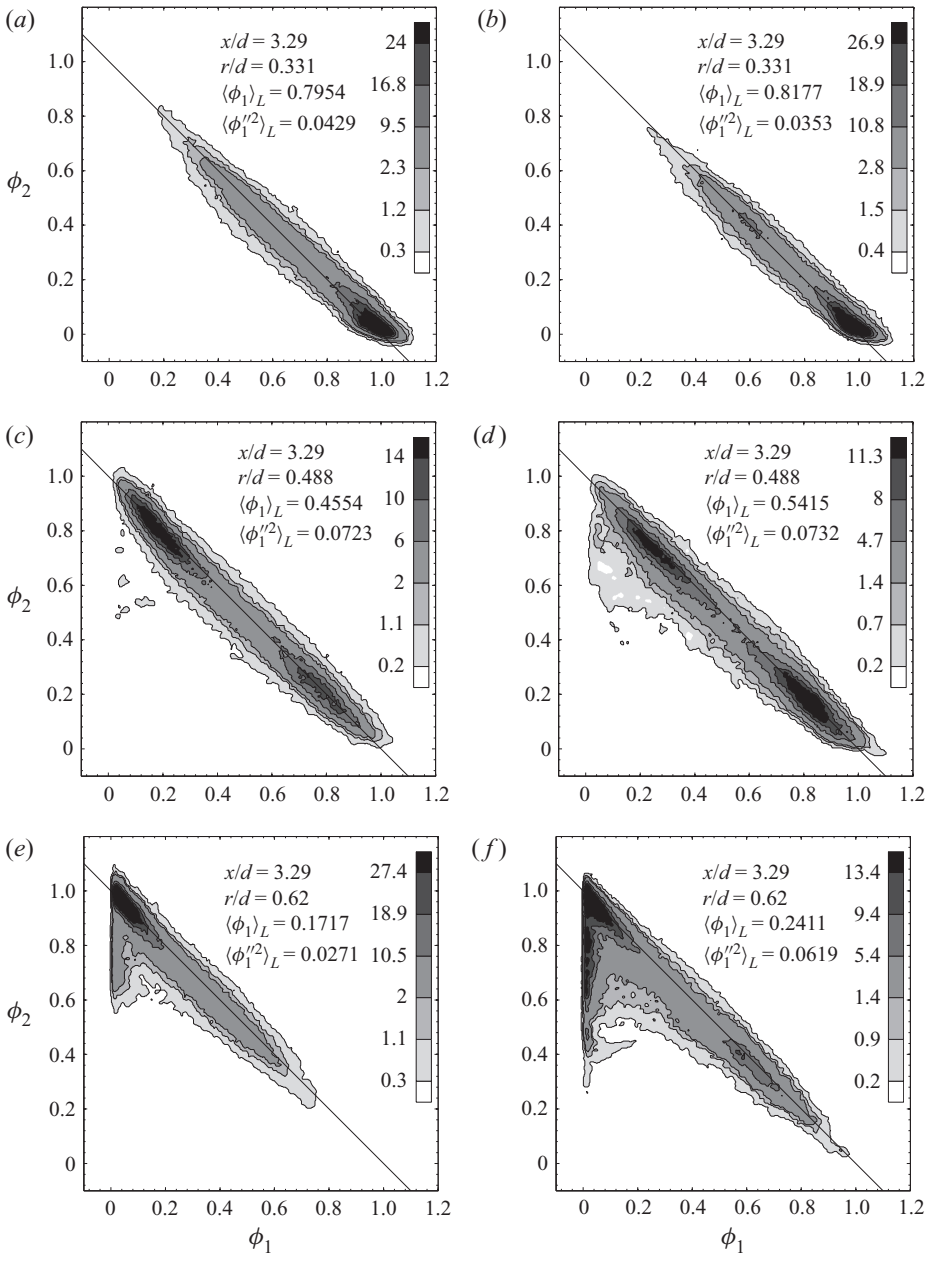

Figure 17. The f.j.d.f. conditional on the large SGS variance at $x/d = 3.29$ for Case III (a,c,e) and Case IV (b,d,f).

with the dissipation rates increasing with ϕ_1. The cross-dissipation also has the same general trend but with positive values.

For large SGS variance, $\langle \chi_1 | \phi_1, \phi_2 \rangle_L$ and $\langle \chi_2 | \phi_1, \phi_2 \rangle_L$ are generally higher than those for small SGS variances. Close to the centreline (not shown), they are higher on the mixing line towards (0, 1). They peak at the location in scalar space where the f.j.d.f. values are low, which indicates that the large dissipation rates are rare events, likely a result

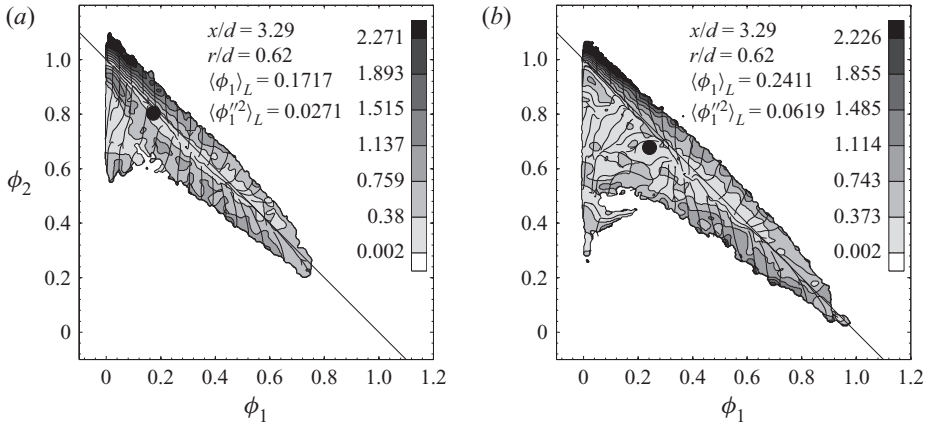

Figure 18. Conditionally filtered diffusion streamlines conditional on the large SGS variance at $x/d = 3.29$ and $r/d = 0.62$ for Case III (a) and Case IV (b).

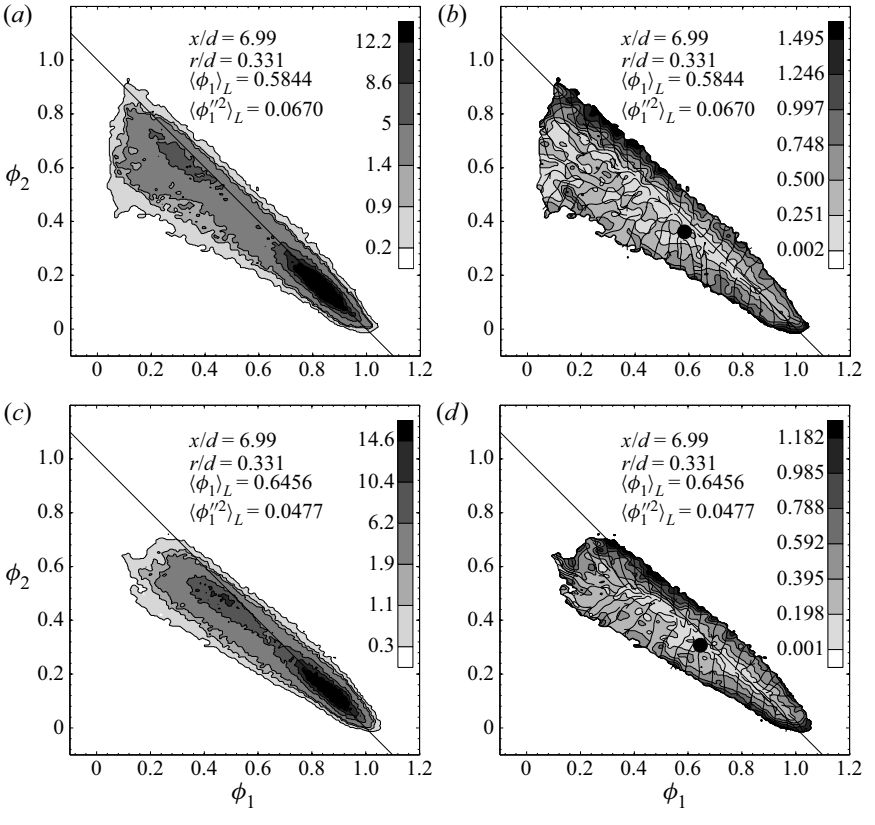

Figure 19. The f.j.d.f. (a,c) and conditionally filtered diffusion streamlines (b,d) conditional on the large SGS variance at $x/d = 6.99$ and $r/d = 0.331$ for Case III (a,b) and Case IV (c,d).

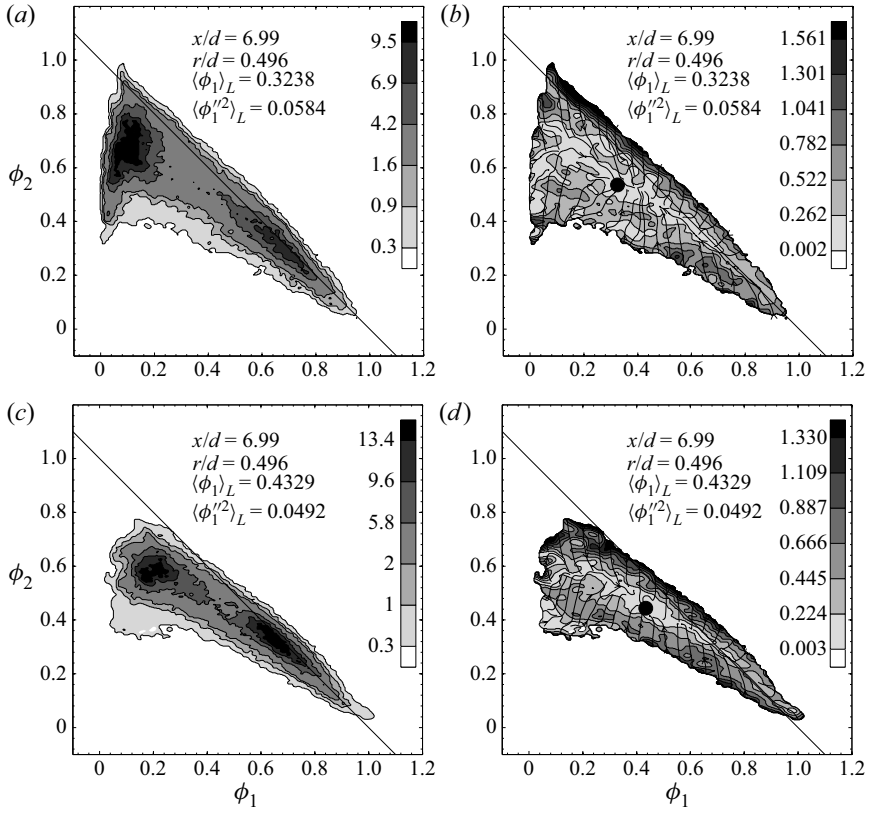

Figure 20. The f.j.d.f. (*a*,*c*) and conditionally filtered diffusion streamlines (*b*,*d*) conditional on the large SGS variance at $x/d = 6.99$ and $r/d = 0.496$ for Case III (*a*,*b*) and Case IV (*c*,*d*).

of strong SGS motions transporting ϕ_2 to this physical location generating a cliff. The cross-dissipation also has the same trend.

At $r/d = 0.372$ (figure 23), $\langle \chi_1 | \phi_1, \phi_2 \rangle_L$ peaks near the lower edge of the f.j.d.f. at intermediate ϕ_1 values, due to the SGS mixing of the ϕ_2–ϕ_3 mixture with ϕ_1. On the ϕ_1–ϕ_2 mixing line, both $\langle \chi_1 | \phi_1, \phi_2 \rangle_L$ and $\langle \chi_2 | \phi_1, \phi_2 \rangle_L$ are higher for intermediate ϕ_1 and ϕ_2 values because this location is near the mean ϕ_1–ϕ_2 interface. For $\langle \chi_2 | \phi_1, \phi_2 \rangle_L$ the peak on the mixing line is higher than that of $\langle \chi_1 | \phi_1, \phi_2 \rangle_L$ due to the higher ethylene diffusivity (the ϕ_1 and ϕ_2 gradients have the same magnitude). The lower edge value of $\langle \chi_2 | \phi_1, \phi_2 \rangle_L$ is lower than the $\langle \chi_1 | \phi_1, \phi_2 \rangle_L$ peak value because the ϕ_2 values are approximately one half of the ϕ_1 value, hence the smaller ϕ_2 gradient and dissipation. The cross-dissipation has a similar trend with negative values. The strengths of the (negative) peaks are between those of $\langle \chi_1 | \phi_1, \phi_2 \rangle_L$ and $\langle \chi_2 | \phi_1, \phi_2 \rangle_L$. The conditionally filtered dissipation rates and cross-dissipation rate for Case II have similar trends (Li *et al.* 2017). However, the peak locations of both $\langle \chi_1 | \phi_1, \phi_2 \rangle_L$ and $\langle \chi_2 | \phi_1, \phi_2 \rangle_L$ for Case II shift to higher ϕ_1 and ϕ_2 values compared with those of Case I.

At $r/d = 0.496$ for Case I (figure 24), $\langle \chi_1 | \phi_1, \phi_2 \rangle_L$ still peak at the lower edge, which indicates that the most intense SGS mixing occurs when large SGS velocity fluctuations bringing together mixtures near the centreline ($\phi_1 = 1$) and far from the centreline (both ϕ_1 and ϕ_2 are low), which produces a ramp–cliff structure. The conditional dissipation, $\langle \chi_1 | \phi_1, \phi_2 \rangle$ (unfiltered), also has a peak near this location (Li *et al.* 2017). The peak of

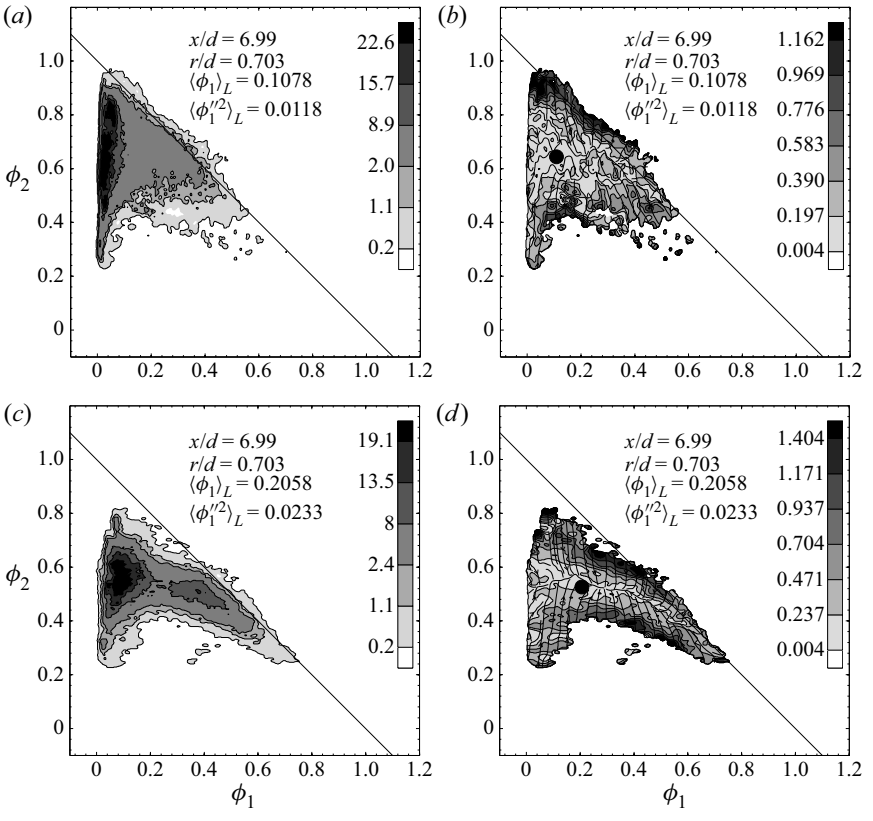

Figure 21. The f.j.d.f. (*a*,*c*) and conditionally filtered diffusion streamlines (*b*,*d*) conditional on the large SGS variance at $x/d = 6.99$ and $r/d = 0.703$ for Case III (*a*,*b*) and Case IV (*c*,*d*).

$\langle \chi_1 | \phi_1, \phi_2 \rangle_L$, however is stronger and exists for a wider range of r/d. Our previous studies (Wang & Tong 2002) have found that in the far field of turbulent round jets the scalar f.d.f. is bimodal and there is a ramp–cliff structure when the SGS variance is large, even when the scalar p.d.f. is unimodal. Thus, the bimodal f.j.d.f. and the peak in the conditionally filtered dissipation is primarily due to the ramp–cliff structure, whereas the bimodal j.p.d.f. is partly due to the flapping of ϕ_1 and the ϕ_2–ϕ_3 mixtures. At this location, $\langle \chi_2 | \phi_1, \phi_2 \rangle_L$ is still large on the mixing line, but with two peaks (the left peak is fairly weak) at the lower edge of the f.j.d.f. These peaks are located on either side of the peak of $\langle \chi_1 | \phi_1, \phi_2 \rangle_L$ in the scalar space. In physical space the peak ϕ_2 is located approximately in the centre part of the ramp–cliff structure, where the ϕ_2 dissipation is small, but on either side of the peak the ϕ_2 gradient is large, which results in two dissipation peaks. The peaks are located in regions of low-ϕ_2 values because for these intense SGS mixing events, the ϕ_2 values are reduced by the co-flow air. The right peak of $\langle \chi_2 | \phi_1, \phi_2 \rangle_L$ is close to the $\langle \chi_1 | \phi_1, \phi_2 \rangle_L$ peak as they likely come from the same mixing events. Their locations (the maximum gradient) do not coincide due to the presence of the co-flow air. For Case II the peaks shift to higher ϕ_2 values, due to the shear layer between the ϕ_1–ϕ_2 streams enhancing mixing without transporting large amounts of ϕ_3.

The conditionally filtered cross-dissipation rate at this location has some of the characteristics of both $\langle \chi_1 | \phi_1, \phi_2 \rangle_L$ and $\langle \chi_2 | \phi_1, \phi_2 \rangle_L$. It has a negative peak close to that of $\langle \chi_1 | \phi_1, \phi_2 \rangle_L$, with magnitudes between those of $\langle \chi_1 | \phi_1, \phi_2 \rangle_L$ and the right peak of

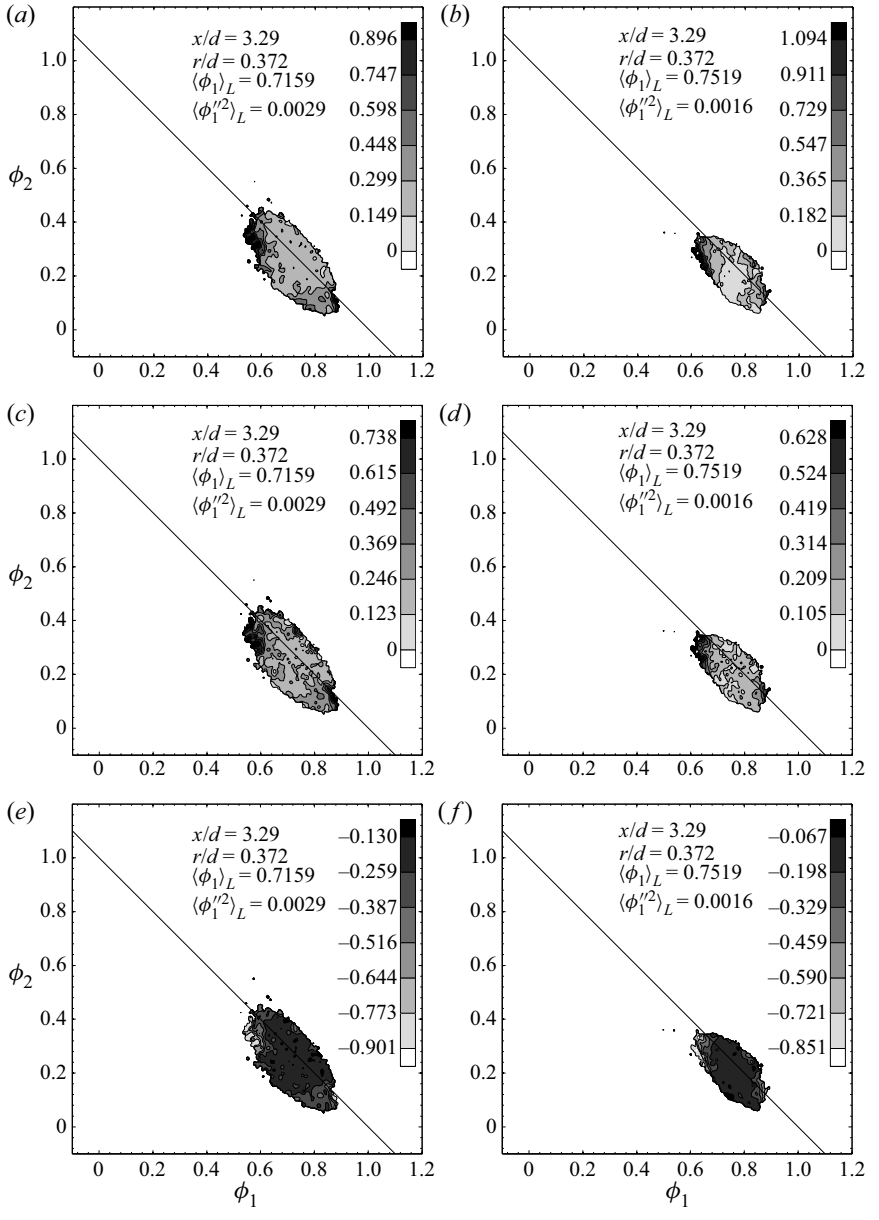

Figure 22. Conditionally filtered dissipation conditional on small SGS variance at $x/d = 3.29$ and $r/d = 0.372$ for Case I (a,c,e) and Case II (b,d,f). (a,b), (c,d), (e,f) are for $\langle\chi_1|\phi_1, \phi_2\rangle_L$, $\langle\chi_2|\phi_1, \phi_2\rangle_L$, and $\langle\chi_{12}|\phi_1, \phi_2\rangle_L$, respectively.

$\langle\chi_2|\phi_1, \phi_2\rangle_L$. It has a positive peak close to that of the left peak of $\langle\chi_2|\phi_1, \phi_2\rangle_L$. Here ϕ_1 and ϕ_2 are being mixed with ϕ_3, hence the positive cross-dissipation. The value, however, is much lower because ϕ_1 and $\langle\chi_1|\phi_1, \phi_2\rangle_L$ are low. The left peaks of both $\langle\chi_2|\phi_1, \phi_2\rangle_L$ and $\langle\chi_{12}|\phi_1, \phi_2\rangle_L$ are stronger for Case I than Case II.

Moving further towards the edge of the jet (not shown), $\langle\chi_1|\phi_1, \phi_2\rangle_L$ and $\langle\chi_2|\phi_1, \phi_2\rangle_L$ have similar trends, each having a peak caused by the ϕ_1–ϕ_2 mixture mixing with ϕ_3.

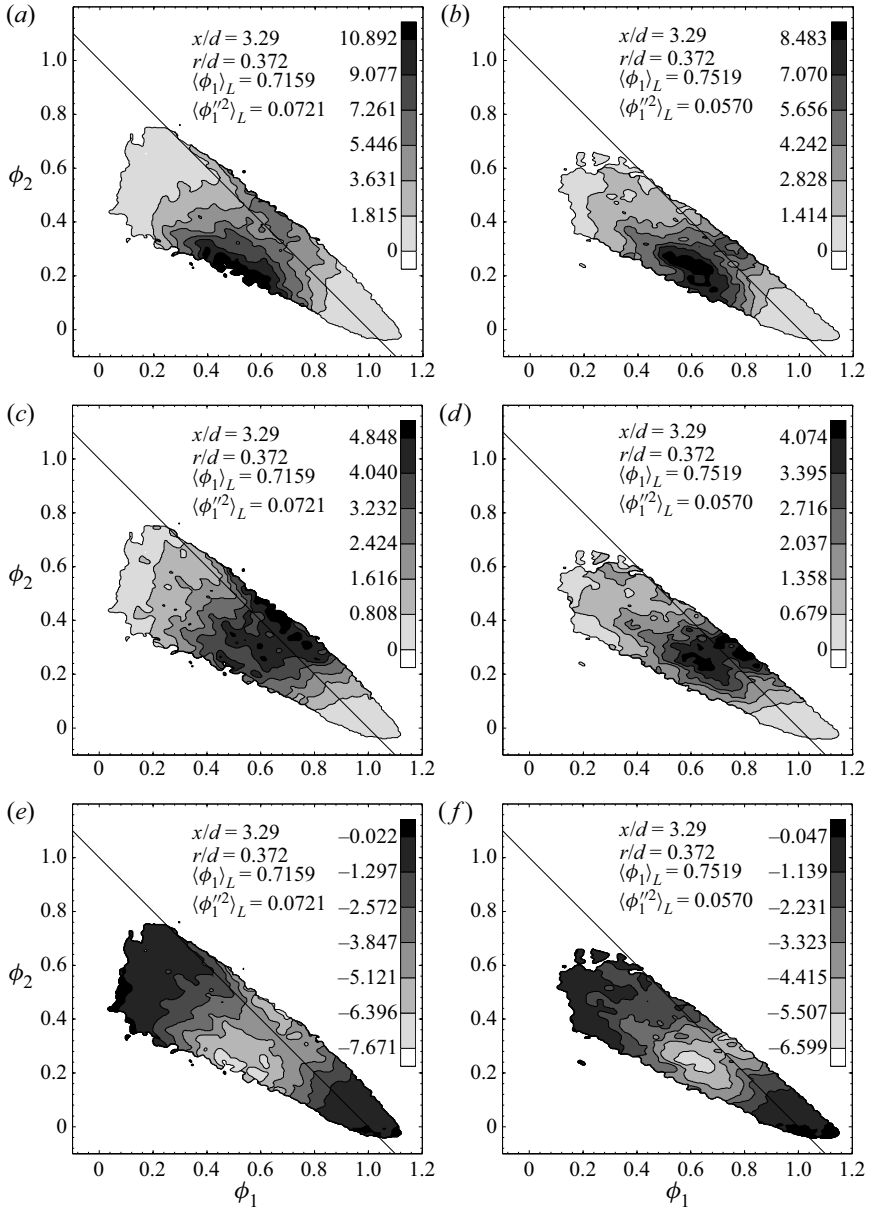

Figure 23. Conditionally filtered dissipation conditional on large SGS variance at $x/d = 3.29$ and $r/d = 0.372$ for Case I (a,c,e) and Case II (b,d,f). (a,b), (c,d), (e,f) are for $\langle \chi_1 | \phi_1, \phi_2 \rangle_L$, $\langle \chi_2 | \phi_1, \phi_2 \rangle_L$, and $\langle \chi_{12} | \phi_1, \phi_2 \rangle_L$, respectively.

The cross-dissipation has the same trend as $\langle \chi_1 | \phi_1, \phi_2 \rangle_L$ and $\langle \chi_2 | \phi_1, \phi_2 \rangle_L$, and has positive values because ϕ_1 and ϕ_2 are well mixed and well correlated at this location.

The general trends for the larger annulus are similar to the smaller annulus. However, the peaks are located at higher ϕ_2 (closer to the ϕ_1–ϕ_2 mixing line) for Case III than for Case IV (e.g. at $x/d = 6.99$ and $r/d = 0.496$ shown in figure 25), which is opposite to the relative locations between Case I and Case II.

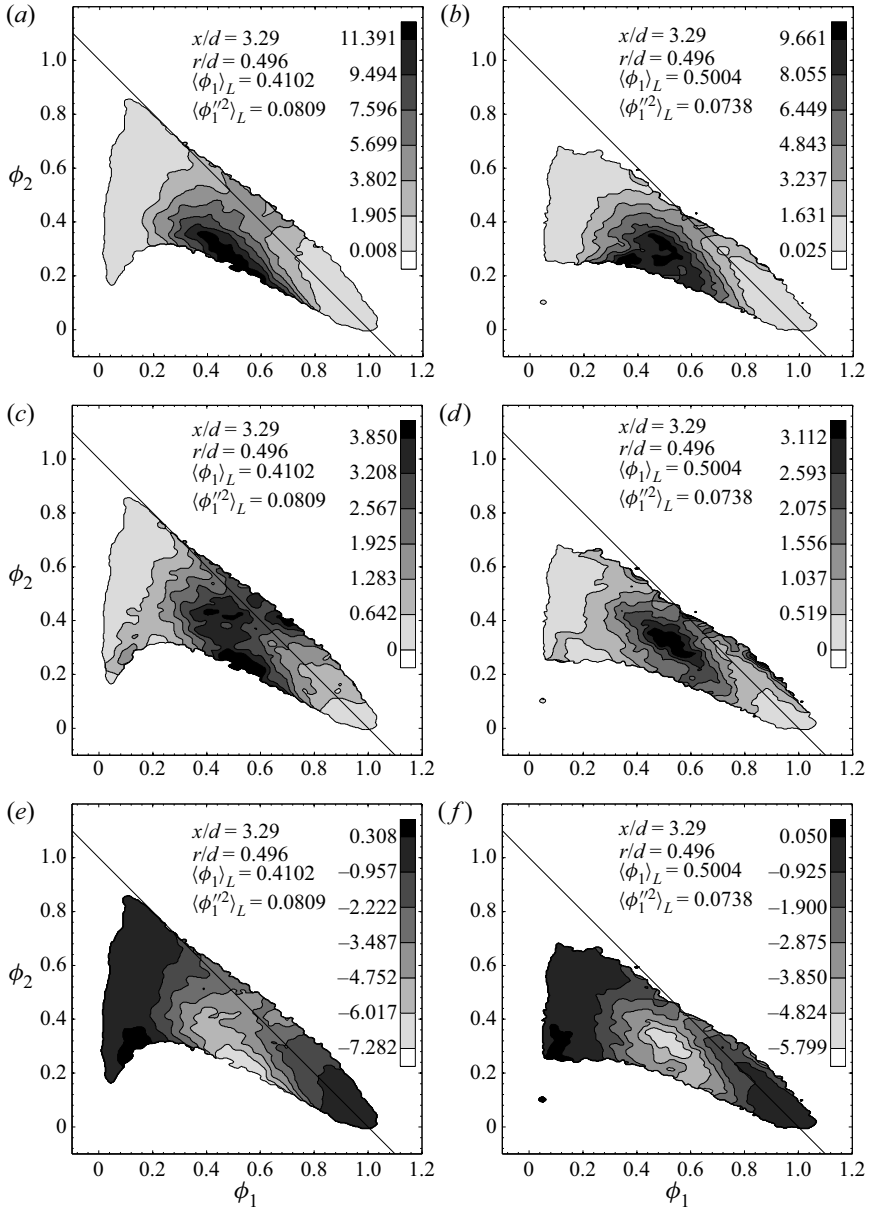

Figure 24. Conditionally filtered dissipation conditional on the large SGS variance at $x/d = 3.29$ and $r/d = 0.496$ for Case I (a,c,e) and Case II (b,d,f). (a,b), (c,d), (e,f) are for $\langle\chi_1|\phi_1, \phi_2\rangle_L$, $\langle\chi_2|\phi_1, \phi_2\rangle_L$, and $\langle\chi_{12}|\phi_1, \phi_2\rangle_L$, respectively.

The results on the conditionally filtered dissipation suggest that there exist several SGS mixing scenarios in the near field of the coaxial jets studied. The first involves mixing of ϕ_1 and a ϕ_2–ϕ_3 mixture, which is probably caused by large SGS velocity fluctuations bringing ϕ_1 and ϕ_3 together, which produces high dissipation rates. The second scenario involves primarily ϕ_1–ϕ_2 mixing, which generally does not require SGS velocity fluctuations as large as in the first scenario. The dissipation rates, therefore, are lower than those in the first scenario. These two scenarios generally occur in most regions of the jet, but with very

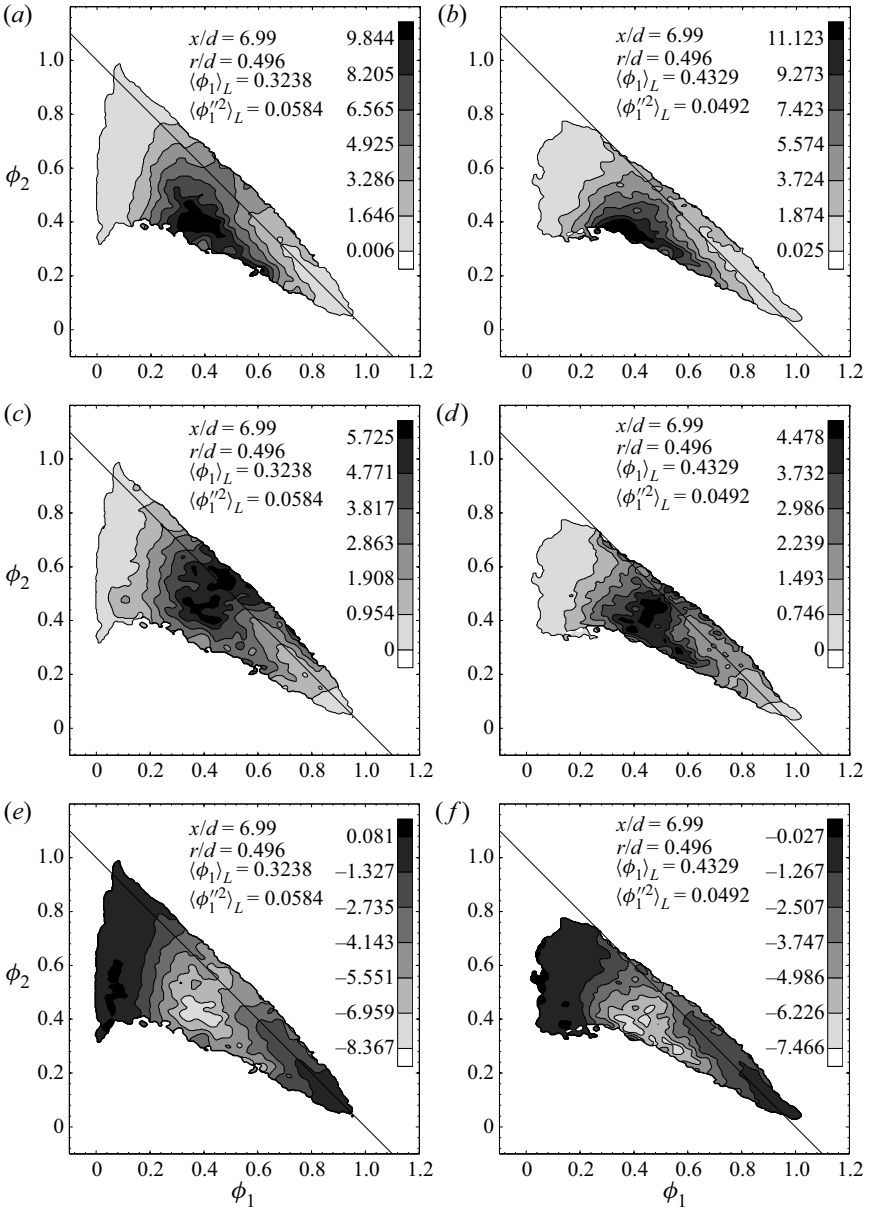

Figure 25. Conditionally filtered dissipation conditional on the large SGS variance at $x/d = 6.99$ and $r/d = 0.496$ for Case III (a,c,e) and Case IV (b,d,f). (a,b), (c,d) and (e,f) are for $\langle\chi_1|\phi_1,\phi_2\rangle_L$, $\langle\chi_2|\phi_1,\phi_2\rangle_L$ and $\langle\chi_{12}|\phi_1,\phi_2\rangle_L$, respectively.

low probabilities towards the edge. The third scenario involves mixing of the ϕ_1–ϕ_2–ϕ_3 mixture with pure ϕ_3, and occurs primarily towards the edge of the jet.

While these mixing scenarios occur under general conditions, they manifest themselves more clearly when the SGS variance is large. For small SGS variance, the SGS scalars are relatively well mixed. The conditionally filtered dissipation rates and their variations in the scalar space are moderate. For large SGS variance, the SGS fields contain the ramp–cliff structure for ϕ_1. The conditionally filtered dissipation rates for both ϕ_1 and ϕ_2 are higher.

In the first SGS mixing scenario, $\langle\chi_1|\phi_1,\phi_2\rangle_L$ has a peak near the centre of the cliff and $\langle\chi_2|\phi_1,\phi_2\rangle_L$ has two peaks, one on each side of the $\langle\chi_1|\phi_1,\phi_2\rangle_L$ peak. These peaks are located in the part of the scalar space with relatively low-ϕ_2 values, since a significant amount of ϕ_3 is brought in by the large SGS velocity fluctuations. In the second scenario the cliff for ϕ_1 is not as sharp as in the first scenario. Thus $\langle\chi_1|\phi_1,\phi_2\rangle_L$ might not have a peak in the scalar space. The overall pattern of the conditionally filtered dissipation rates are largely determined by the relative probability and the dissipation magnitudes of these SGS mixing scenarios.

The results also show that $\langle\chi_2|\phi_1,\phi_2\rangle_L$ has some similarities to the conditionally filtered temperature dissipation in a turbulent non-premixed flame. There are two $\langle\chi_2|\phi_1,\phi_2\rangle_L$ peaks, one on each side of the peak of $\langle\chi_1|\phi_1,\phi_2\rangle_L$. These peaks are near the lower edge of the f.j.d.f., due to the large dissipation lowering the ϕ_2 values. In flames, high temperatures are generated between mixture fraction values of one (fuel stream, similar to $\phi_1 = 1$) and zero (air stream), thus having a similar mixing configuration as the three-scalar mixing in the present turbulent coaxial jet. The conditionally filtered temperature dissipation has peaks on both sides of the peak temperature in the scalar space (Cai *et al.* 2009). Due to the heat release generating high temperatures, the locations of peaks relative to the f.j.d.f. peaks in the mixture fraction–temperature space are much higher than those of the $\langle\chi_2|\phi_1,\phi_2\rangle_L$ in the ϕ_1–ϕ_2 f.j.d.f. domain. The temperature dissipation for the locally extinguished samples are more similar to $\langle\chi_2|\phi_1,\phi_2\rangle_L$ in the present study due to the lack of a temperature source.

4. Conclusions and further discussion

The present work investigated experimentally three-scalar SGS mixing in turbulent coaxial jets. An important and unique aspect of this flow is that the centre jet and the co-flow air are separated by the annular flow, which results in a mixing configuration similar to that of the mixture fraction and temperature (or a major product) in a turbulent non-premixed and partially premixed flame. The three-scalar SGS mixing process, therefore, better approximates the multiscalar SGS mixing process in a turbulent reactive flow.

The fundamental characteristics of SGS mixing and its dependence on the SGS variance and the mean shear and scalar initial length scale were investigated in detail, using the conditional means of the scalar f.j.d.f., the conditionally filtered scalar diffusion, dissipation and cross-dissipation. The filtered scalar and the SGS scalar variance of the centre jet (ϕ_1) are used as the conditioning variables. The results show that similar to binary SGS mixing in the fully developed turbulent scalar fields, there are also two SGS mixing regimes for the three-scalar mixing in turbulent coaxial jets. For small SGS variance the scalars are well mixed. The f.j.d.f. is unimodal; therefore, the initial three-scalar mixing configuration is lost. In a non-premixed turbulent flame, the loss of the mixing configuration could have strong implications for the structure of the reaction zones. The diffusion streamlines representing the conditionally filtered diffusion approach a stagnation point directly. The conditionally filtered scalar dissipation and cross-dissipation rates are low and their variations are small.

For large SGS variance, the scalars are highly segregated and the scalar structure (mixing configuration) in both the scalar space and physical space is similar to the initial scalar structure (configuration), in contrast to the small SGS variance for which the initial three-scalar mixing configuration is lost. The f.j.d.f. is bimodal near the peak location of the mean SGS variance of ϕ_1 for all cases. The bimodal f.j.d.f. is a result of two competing factors, the SGS variance and the scalar length scale. For the higher velocity

ratio cases a larger SGS variance in the neighbourhood of the peak mean SGS variance causes stronger bimodality, while for the smaller velocity ratio cases the smaller scalar length scale and the wider mean SGS variance profile cause bimodal f.j.d.f. over a wider range of physical locations. The diffusion streamlines first converge to a manifold in the scalar space and continue on it towards a stagnation point. The manifold provides a mixing path for the centre jet scalar and the co-flow air. The curvature of the diffusion manifold is larger for higher velocity ratio cases, which indicates slower SGS mixing processes. The conditionally filtered scalar dissipation rates and cross-dissipation rate are consistent with those produced by the large SGS scalar structures. They also reveal several SGS mixing scenarios in which the largest SGS scales of the velocity field are likely to play a key role. These SGS mixing characteristics present a challenging test for SGS mixing models as well as an understanding of the physics for developing improved SGS mixing models. The scalar dissipation rate structures for ϕ_1 and ϕ_2 have similarities to those of mixture fraction and temperature in turbulent non-premixed/partially premixed flames. The results in the present work, therefore, also provide a basis for investigating and understanding multiscalar SGS mixing in turbulent flames.

The f.j.d.f. studied in this paper also provides a basis and an impetus for investigating three-scalar mixing in the context of a new LES approach proposed by Fox (2003) and systematically developed by Pope (2010). The approach is based on the concept of self-conditioned fields, e.g. the scalar j.p.d.f. conditioned on a reduced representation of the scalar fields that can be obtained from the self-conditioned j.p.d.f. The conditional scalar f.j.d.f. can be obtained by filtering the self-conditioned j.p.d.f., which retains some physical-space structure for scales smaller than the LES filter. Therefore, the self-conditioned fields approach is a more general LES approach, which we will investigate in our future studies.

Funding. The work at Clemson was supported by the National Science Foundation under grant CBET-1333489.

Declaration of interests. The authors report no conflict of interest.

Author ORCIDs.
Mengyuan Yuan https://orcid.org/0000-0002-4712-7231;
Chenning Tong https://orcid.org/0000-0002-3086-5027.

References

Antonopoulos-Domis, M. 1981 Large-eddy simulation of a passive scalar in isotropic turbulence. *J. Fluid Mech.* **104**, 55–79.

Cai, J., Barlow, R.S., Karpetis, A.N. & Tong, C. 2011*a* Conditionally filtered diffusion of mixture fraction and temperature in turbulent partially premixed flames. *Proc. Combust. Inst.* **33**, 1505–1513.

Cai, J., Dinger, J.M., Li, W., Carter, D.C., Ryan, D.M. & Tong, C. 2011*b* Experimental study of three-scalar mixing in a turbulent coaxial jet. *J. Fluid Mech.* **685**, 495–531.

Cai, J., Wang, D., Tong, C., Barlow, R.S. & Karpetis, A.N. 2009 Investigation of subgrid-scale mixing of mixture fraction and temperature in turbulent partially premixed flames. *Proc. Combust. Inst.* **32**, 1517–1525.

Colucci, P.J., Jaberi, F.A., Givi, P. & Pope, S.B. 1998 Filtered density function for large eddy simulation of turbulent reacting flows. *Phys. Fluids* **10**, 499–515.

Eswaran, V. & Pope, S.B. 1988 Direct numerical simulations of the turbulent mixing of a passive scalar. *Phys. Fluids* **31** (3), 506–520.

Fox, R.O. 2003 *Computational Models for Turbulent Reactive Flows*. Cambridge University Press.

Frank, J.H., Kaiser, S.A. & Long, M.B. 2002 Reaction rate, mixture fraction, and temperature imaging in turbulent methane/air jet flames. *Proc. Combust. Inst.* **29**, 2687–2694.

GICQUEL, L.Y.M., GIVI, P., JABERI, F.A. & POPE, S.B. 2002 Velocity filtered density function for large eddy simulation of turbulent flows. *Phys. Fluids* **14**, 1196–1213.
HALL, P. 1990 Using the bootstrap to estimate mean squared error and select smoothing parameter in nonparametric problems. *J. Multivar. Anal.* **32**, 177–203.
HOLZER, M. & SIGGIA, E.D. 1994 Turbulent mixing of a passive scalar. *Phys. Fluids* **6**, 1820–1837.
JABERI, F.A., COLUCCI, P.J., JAMES, S., GIVI, P. & POPE, S.B. 1999 Filtered mass density function for large eddy simulation of turbulent reacting flows. *J. Fluid Mech.* **401**, 85–121.
JAYESH, & WARHAFT, Z. 1992 Probability distribution, conditional dissipation, and transport of passive temperature fluctuations in grid-generated turbulence. *Phys. Fluids* A **4**, 2292–2307.
JUNEJA, A. & POPE, S.B. 1996 A dns study of turbulent mixing of two passive scalars. *Phys. Fluids* **8**, 2161–2184.
LI, W., YUAN, M., CARTER, C.D. & TONG, C. 2017 Effects of mean shear and scalar initial length scale on three-scalar mixing in turbulent coaxial jets. *J. Fluid Mech.* **817**, 183–216.
LIU, S. & TONG, C. 2013 Subgrid-scale mixing of mixture fraction, temperature, and species mass fractions in turbulent partially premixed flames. *Proc. Combust. Inst.* **34**, 1231–1239.
MA, B. & WARHAFT, Z. 1986 Some aspects of the thermal mixing layer in grid turbulence. *Phys. Fluids* **29**, 3114–3120.
OVERHOLT, M.R. & POPE, S.B. 1996 Direct numerical simulation of a passive scalar with imposed mean gradient in isotropic turbulence. *Phys. Fluids* **8**, 3128–3148.
POPE, S.B. 2010 Self-conditioned fields for large-eddy simulations of turbulent flows. *J. Fluid Mech.* **652**, 139–169.
POPE, S.B. 1990 Computations of turbulent combustion: Progress and challenges. In *Proceedings of the 23rd Symposium (International) on Combustion*, pp. 591–612. The Combustion Institute.
POPE, S.B. 2000 *Turbulent Flows*. Cambridge University Press.
PRAUSNITZ, J.M., POLING, B.E. & O'CONNELL, J.P. 2001 *The Properties of Gases and Liquids*. McGraw Hill.
RAJAGOPALAN, A.G. & TONG, C. 2003 Experimental investigation of scalar-scalar-dissipation filtered joint density function and its transport equation. *Phys. Fluids* **15**, 227–244.
RAMAN, V., PITSCH, H. & FOX, O.R. 2005 Hybrid large-eddy simulation/lagrangian filtered-density-function approach for simulating turbulent combustion. *Combust. Flame* **143**, 56–78.
REID, R.C., PRAUSNITZ, J.M. & POLING, B.E. 1989 *The Properties of Gases and Liquids*. McGraw Hill.
ROWINSKI, D.H. & POPE, S.B. 2013 An investigation of mixing in a three-stream turbulent jet. *Phys. Fluids* **25**, 105105.
RUPPERT, D. 1997 Empirical-bias bandwidths for local polynomial nonparametric regression and density estimatio. *J. Am. Stat. Assoc.* **92**, 1049–1062.
SHEIKHI, M.R.H., DROZDA, T.G., GIVI, P., JABERI, F.A. & POPE, S.B. 2005 Large eddy simulation of a turbulent nonpremixed piloted methane jet flame (sandia flame d). *Proc. Combust. Inst.* **30**, 549–556.
SHEIKHI, M.R.H., DROZDA, T.G., GIVI, P. & POPE, S.B. 2003 Velocity-scalar filtered density function for large eddy simulation of turbulent flows. *Phys. Fluids* **15**, 2321–2337.
SHETTY, D.A., CHANDY, A.J. & FRANKEL, S.H. 2010 A new fractal interaction by exchange with the mean mixing model for large eddy simulation/filtered mass density function applied to a multiscalar three-stream turbulent jet. *Phys. Fluids* **22**, 025102.
SIRIVAT, A. & WARHAFT, Z. 1982 The mixing of passive helium and temperature fluctuations in grid turbulence. *J. Fluid Mech.* **120**, 475–504.
SREENIVASAN, K.R., TAVOULARIS, S., HENRY, R. & CORRSIN, S. 1980 Temperature fluctuations and scales in grid-generated turbulence. *J. Fluid Mech.* **100**, 597–621.
TONG, C. 2001 Measurements of conserved scalar filtered density function in a turbulent jet. *Phys. Fluids* **13**, 2923–2937.
TONG, C. & WARHAFT, Z. 1994 On passive scalar derivative statistics in grid turbulence. *Phys. Fluids* **6**, 2165–2176.
TONG, C. & WARHAFT, Z. 1995 Scalar dispersion and mixing in a jet. *J. Fluid Mech.* **292**, 1–38.
WAND, M.P. & JONES, M.C. 1995 *Kernel Smoothing*. Chapman & Hall.
WANG, D. & TONG, C. 2002 Conditionally filtered scalar dissipation, scalar diffusion, and velocity in a turbulent jet. *Phys. Fluids* **14**, 2170–2185.
WANG, D. & TONG, C. 2005 Experimental study of velocity-scalar filtered joint density function for les of turbulent combustion. *Proc. Combust. Inst.* **30**, 567–574.
WANG, D., TONG, C., BARLOW, R.S. & KARPETIS, A.N. 2007*a* Experimental study of scalar filtered mass density function in turbulent partially premixed flames. *Proc. Combust. Inst.* **31**, 1533–1541.

WANG, G., KARPETIS, A.N. & BARLOW, R.S. 2007*b* Dissipation length scales in turbulent nonpremixed jet flames. *Combust. Flame* **148**, 62–75.

WARHAFT, Z. 1981 The use of dual heat injection to infer scalar covariance decay in grid turbulence. *J. Fluid Mech.* **104**, 93–109.

WARHAFT, Z. 1984 The interference of thermal fields from line sources in grid turbulence. *J. Fluid Mech.* **144**, 363–387.

WARHAFT, Z. & LUMLEY, J.L. 1978 An experimental study of the decay of temperature fluctuations in grid-generated tubulence. *J. Fluid Mech.* **88**, 659–684.